Chapter 4

Multi-Core Optical Fibers: Theory, Applications and Opportunities

Andrés Macho Ortiz and Roberto Llorente Sáez

Additional information is available at the end of the chapter

http://dx.doi.org/10.5772/intechopen.72458

Abstract

Multi-core fibers (MCFs) have sparked a new paradigm in optical communications, as they can significantly increase the Shannon capacity of optical networks based on single-core fibers. In addition, MCFs constitute a useful platform for testing different physical phenomena, such as quantum or relativistic effects, as well as to develop interesting applications in various fields, such as biological and medical imaging. Motivated by the potential applications of these new fibers, we will perform a detailed review of the MCF technology including a theoretical analysis of the main physical impairments and new dispersive effects of these fibers, and we will discuss their emerging applications and opportunities in different branches of science.

Keywords: multi-core fiber, inter-core crosstalk, birefringent effects, intermodal dispersion, microwave photonics, optical sensors, medical imaging

1. Introduction

Data traffic demand in access and backbone networks has been increased exponentially in the last three decades [1, 2]. Remarkably, in the last decade, the development of streaming transmissions and cloud computing has accelerated this growth [3]. Nowadays, in spite of the fact that this data traffic demand is easily covered by wavelength-division multiplexed (WDM) systems based on single-mode single-core fibers (SM-SCFs),[1] recent works show that the WDM systems are rapidly approaching their Shannon capacity limit [4].

Aimed to overcome the Shannon capacity limit of WDM networks using SM-SCFs, space-division multiplexing (SDM) has been extensively investigated in recent years [5–7].

[1] SM-SCFs are also termed in the literature as single-mode fibers (SMFs).

Remarkably, the SDM concept within the context of optical communications was proposed for the first time in the decade of 1980 [8–10]. Unfortunately, the technology underneath SDM was immature and extremely expensive. Nevertheless, the fabrication methods of the SDM fibers and optical devices have been extensively developed in the last decade reducing their manufacturing cost [11]. In this scenario, new types of optical fibers based on the SDM concept have been proposed [5–12]: fiber bundle based on SM-SCFs, multi-mode single-core fibers (MM-SCFs),[2] single/multi-mode multi-core fibers (SM/MM-MCFs) and photonic crystal fibers.

In contrast with the other aforementioned SDM fibers, MCFs allow us to increase the channel capacity limit of SM-SCFs by exploiting the six signal dimensions (time, wavelength, amplitude, phase, polarization and space) through spatial multi-dimensional modulation formats and digital signal processing at the receiver [13–15]. Interestingly, SCFs have also been used as an experimental platform for testing different phenomena related to diverse branches of physics, such as fluid dynamics, quantum mechanics, general relativity and condensed matter physics, as well as to develop applications in other fields [16–23]. Along this line, MCFs are potential laboratories that could extend the possibilities offered by SCFs. As an example, disordered MCFs exhibiting transverse Anderson localization have been proposed with potential applications in biological and medical imaging [22].

Inspired by the potential applications of these new fibers, we perform a detailed review of the MCF technology including a theoretical analysis of the main physical impairments and new dispersive effects of these fibers, and we discuss their applications and opportunities in different branches of physics, engineering and medicine. The chapter is organized as follows. In Section II, the different MCF types are revisited. In Section III, we include some fundamental aspects of light propagation in the linear and nonlinear fiber regime. Specifically, we focus on the theoretical description of the physical impairments observed in these fibers in the single-mode regime: the linear and nonlinear inter-core crosstalk, the intra- and inter-core birefringent effects, the intermodal dispersion and higher-order coupling and nonlinear effects. In Section IV we discuss the main applications and opportunities of MCFs in photonics, medicine and experimental physics. Finally, in Section V the main conclusions of the chapter and the open research lines in the topic are highlighted.

2. Multi-core fiber types and fabrication

MCF designs can be classified in different categories attending to diverse fiber parameters and characteristics. **Table 1** shows the usual MCF designs employed for SDM transmissions and MCF laser and sensing applications:

1. The refractive index profile of each core allows us to differentiate between step-index (SI-MCF) and gradual-index MCFs (GI-MCF). In the former case, the refractive index profile of all cores has a step between two constant values in the core and cladding interface. However, in the latter case, a MCF is referred to as GI-MCF if at least one core

[2] MM-SCFs are also referred to as multi-mode fibers (MMFs).

has a continuous refractive index profile. Along this line, we can make a distinction with a third type of MCF: a trench- or hole-assisted MCF (TA-MCF or HA-MCF). In general, a TA- and HA-MCF present a multi-step refractive index profile in the cladding to reduce the mode-coupling (inter-core crosstalk) between the linearly polarized (LP) modes of adjacent cores [7, 11, 12, 24]. Specifically, in a HA-MCF an additional step is included in the cladding by performing holes around the cores [7].

MCF classification	**Type 1**	**Type 2**	**Figure/comments**
Refractive index profile	Step-index SI-MCF	Gradual-index GI-MCF	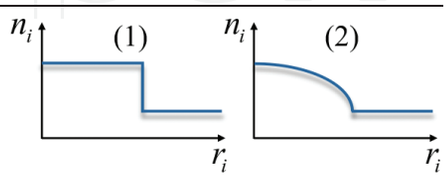
Modal regime	Single-mode SM-MCF	Multi-mode MM-MCF	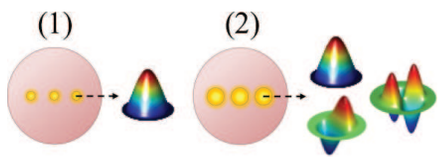
Spatial homogeneity	Homogeneous cores HO-MCF	Heterogeneous cores HE-MCF	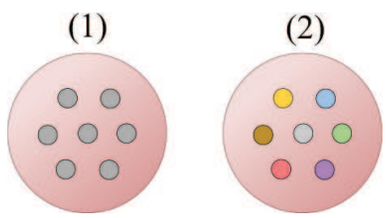
Core-to-core distance (d_{ab})	Uncoupled cores ($d_{ab} \geq 7 \cdot R_0$) UC-MCF	Coupled cores ($d_{ab} < 7 \cdot R_0$) CC-MCF	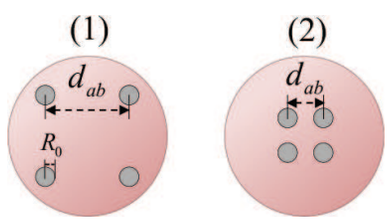
Intrinsic linear birefringence	Lowly birefringent cores LB-MCF	Highly birefringent cores HB-MCF	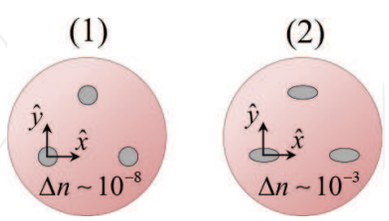
Others	(1) Trench-assisted MCF (TA-MCF), (2) Hole-assisted MCF (HA-MCF), (3) MCF with coupled and uncoupled cores, (4) Dispersion-shifted MCF (DS-MCF), (5) MCF Bragg gratings, (6) Hexagonal shaped cores…		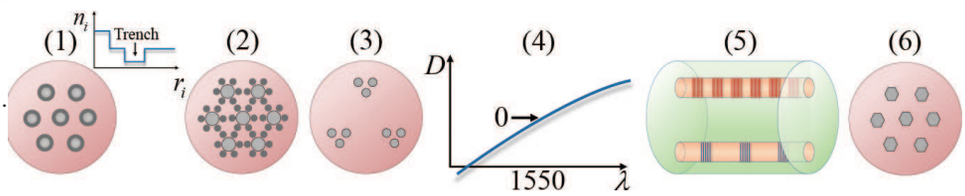

Table 1. Classification of multi-core fiber types.

2. A single-mode MCF (SM-MCF) supports only the LP_{01} mode in each core. In contrast, if a given core guides several LP modes, the fiber is known as a multi-mode MCF (MM-MCF). Moreover, a MCF supporting only the first three or four LP mode groups (LP_{01}, LP_{11}, LP_{21}, LP_{02}) is usually termed as a few-mode MCF (FM-MCF) [7].

3. Attending to the spatial homogeneity of the MCF structure, we can make a distinction between a homogeneous MCF (HO-MCF) or a heterogeneous MCF (HE-MCF). In the former case, all cores present the same refractive index profile, and in the latter case, the MCF comprises at least one core with a different refractive index profile[3].

4. The core-to-core distance (or core pitch) is the main fiber parameter which determinates the inter-core crosstalk level among the LP modes of each core. Usually, if the core pitch between two homogeneous cores a and b (d_{ab}) is lower than seven times[4] the core radius R_0, the LP modes of the cores are found to be degenerated and the MCF supports supermodes [25]. In such a case, the MCF is referred to as a coupled-core MCF (CC-MCF). On the contrary, if the LP modes of the cores a and b are non-degenerated, the supermodes cannot be generated and each core is considered as an individual light path. This fiber design is termed as uncoupled-core MCF (UC-MCF). Recent works have reported a mixed design using coupled and uncoupled cores [26, 27].

5. If the intrinsic linear birefringence of each core $\Delta n = |n_x - n_y|$ is lower than 10^{-7}, the MCF is referred to as lowly birefringent MCF (LB-MCF). Nonetheless, if a given core has a $\Delta n > 10^{-7}$ the MCF is known as a highly birefringent MCF (HB-MCF). In general, a HB-MCF comprises elliptical or panda cores for polarization-maintaining applications [28, 29].

6. Other designs of MCFs involve: dispersion-shifted cores (DS-MCFs) [30], selective-inscribed Bragg gratings [31] and hexagonal shaped cores [32].

Once the MCF cross-section design is established, the specific MCF fabrication method is of key importance for the final optical transmission characteristics. MCF fabrication processes have been refined and optimized in the last years with an intensive research work [5, 7, 33–37]. In this scenario, the main technological challenge in the design and fabrication of uncoupled MCFs is to minimize the crosstalk providing the maximum core isolation. Usually, the design work is performed numerically using commercial simulation packages. The simulation analysis targets to determine the cross-section modal distribution, the spectral power density of the LP modes, the associated power losses and the resulting inter-core crosstalk.

MCF fabrication can be addressed by microstructured stack-and-draw technology [36], a flexible technology which allows us to fabricate very different fibers on the same machinery. Unfortunately, MCF manufacturing is a complex process with nonlinear results on the process parameters. In particular, some rods or capillaries configurations may be technically difficult to draw into the designed form, which results in a MCF with higher crosstalk levels than in the

[3]Two cores a and b have a different refractive index profile if $n_a(r_a) \neq n_b(r_b)$, where $r_{a(b)}$ is the local radial coordinate of each core. Hence, two step-index cores have a different refractive index profile if $n_a(r_a = 0) \neq n_b(r_b = 0)$.

[4]The condition $d_{ab} < 7R_0$ is only an approximation in the third transmission window and in single-mode regime of each core, with $R_0 \sim 4$ μm. In general, the criteria to achieve the supermode regime in the MCF structure depend on additional fiber parameters such as the refractive index profile and the wavelength of the optical carrier.

original design. In this scenario, it is necessary to investigate the linear and nonlinear MCF propagation taking into account not only the MCF manufacturing imperfections, but also additional external fiber perturbations (see below). This would be of great benefit for investigating multi-dimensional modulation formats, spatial encoding techniques and sharing of receiver resources in MCF systems [38–41].

3. Linear and nonlinear propagation in real MCFs

In general, the electromagnetic analysis of a MCF should be performed by solving the macroscopic Maxwell equations (MMEs) in each dielectric region of the fiber (cores + cladding) and applying the boundary conditions between the cores-cladding interfaces. However, the calculation of the exact MCF eigenmodes from the MMEs presents a high degree of complexity, and usually, they should be calculated numerically. Therefore, in order to analyze theoretically the electromagnetic phenomena in MCF media, the perturbation theory is usually employed. **Figure 1** shows a flowchart of this approach.

The goal is to derive a set of coupled equations from the MMEs in terms of the complex envelopes of the electric field strength in each core performing the next steps:

1. First, we should propose the ansatz of the global electric field strength ($\boldsymbol{\mathcal{E}}$) of the MCF structure following the assumption of the classical perturbation theory [42]: the exact electric field strength is approximated by a linear combination of the *mi* polarized core modes[5] considering isolated cores, that is, assuming that the geometry of each core *m* is not perturbed by the presence of adjacent cores [$\boldsymbol{\mathcal{E}} \approx \sum \boldsymbol{\mathcal{E}}_{mi}$]. At the same time, we should decouple the rapid- and the slowly varying temporal and longitudinal changes of $\boldsymbol{\mathcal{E}}_{mi}$. The

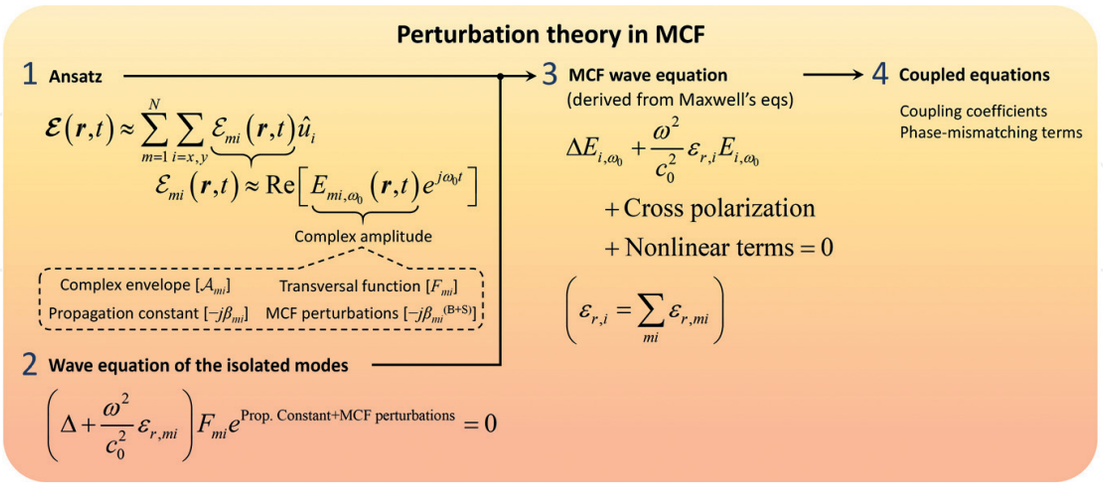

Figure 1. Flowchart of the perturbation theory in MCF media to derive the coupled equations from the macroscopic Maxwell equations.

[5]The polarized core mode *mi* refers to the $LP_{01,mi}$ mode associated with core *m* and polarization axis *i*.

rapidly varying temporal changes are decoupled by using the slowly varying complex amplitude approximation with $\boldsymbol{\mathcal{E}}_{mi}(\boldsymbol{r},t) \approx f(E_{mi,\omega 0}(\boldsymbol{r},t))$, where $E_{mi,\omega 0}$ is the complex amplitude and ω_0 is the angular frequency of the optical carrier[6]. In a similar way, the rapidly varying longitudinal variations are decoupled by writing $E_{mi,\omega 0}$ as a function of the complex envelopes $\mathcal{A}_{mi}(z,t)$, that is, $E_{mi,\omega 0}(\boldsymbol{r},t) \approx f(\mathcal{A}_{mi}(z,t))$. Although ε_{mi} is written assuming isolated conditions, the complex envelopes should be assumed longitudinal dependent to describe not only the usual longitudinal distortion[7] of the optical pulses in SM-SCFs, but also the longitudinal fluctuations induced by the mode-coupling. Moreover, $E_{mi,\omega 0}$ also involves fundamental information such as the ideal propagation constant ($-j\beta_{mi}$), the transversal eigenfunction (F_{mi}) and the MCF perturbations [bending, twisting and additional fiber birefringent fluctuations modeled by the longitudinal and temporal dependent phase function $\beta_{mi}{}^{B+S}(z,t)$][8].

2. Each polarized core mode $\boldsymbol{\mathcal{E}}_{mi}$ is written by assuming isolated conditions of each core. Therefore, the transversal eigenfunction F_{mi} and the ideal phase constant β_{mi} can be expressed as indicated in [44] for the LP_{01} mode of a single-core fiber. Moreover, taking into account that the nonlinear effects are not included in the modal solution of [44] and in the MCF perturbations $\beta_{mi}{}^{B+S}$, thus the eigenfunction $F_{mi}\cdot\exp(-j(\beta_{mi} + \beta_{mi}{}^{B+S})z)$ should satisfy the linear wave equation in each core and polarization in $\delta z \sim \lambda_0$, where λ_0 is the maximum value of the wavelength of the optical carrier in the multi-dielectric medium[9].

3. In the third step, the wave equation of the MCF should be derived for the complex amplitudes $E_{mi,\omega 0}$ from the MMEs by taking into account the cross- and nonlinear polarization.

4. Finally, using the results of the first and second step in the MCF wave equation, we finally derive the coupled equations of the complex envelopes by assuming the slowly varying complex envelope approximation (SVEA), that is, $\delta_z\mathcal{A}_{mi} << |\mathcal{A}_{mi}|$ in $\delta z \sim \lambda_0$ and $\delta_t\mathcal{A}_{mi} << |\mathcal{A}_{mi}|$ in $\delta t \sim 2\pi/\omega_0$. More specifically[10]:

$$\left|\frac{\partial^2\mathcal{A}_{mi}}{\partial z^2}\right| \ll k_0\left|\frac{\partial\mathcal{A}_{mi}}{\partial z}\right| \ll k_0^2|\mathcal{A}_{mi}|; \quad \left|\frac{\partial^2\mathcal{A}_{mi}}{\partial t^2}\right| \ll \omega_0\left|\frac{\partial\mathcal{A}_{mi}}{\partial t}\right| \ll \omega_0^2|\mathcal{A}_{mi}|, \tag{1}$$

where $k_0 = 2\pi/\lambda_0$. Thus, we can approximate $\partial_z{}^2\mathcal{A}_{mi} \approx 0$.

In the following subsections, we will review the new physical impairments observed in SM-MCFs using the aforementioned perturbation theory. First, we will describe the inter-core

---

[6] In general, we cannot consider a single-optical carrier in SDM-WDM systems using SM-MCFs. However, the interchannel nonlinearities should only be taken into account for optical pulses higher than 50 ps [43]. Therefore, the assumption of a single-optical carrier allows us to investigate the major physical impairments in SM-MCFs.

[7] Chromatic dispersion, polarization-mode dispersion and additional distortions induced by the intra-core nonlinear effects.

[8] In Section 3.1, we will be more specific with the description of the MCF perturbations.

[9] The symbol λ_0 is commonly used in the literature to describe the wavelength of the optical carrier at the vacuum. The context should avoid any confusion.

[10] Note that $\delta_z\mathcal{A}_{mi}$ and $\delta_t\mathcal{A}_{mi}$ are defined as $\delta_z\mathcal{A}_{mi} := |\mathcal{A}_{mi}(z,t) - \mathcal{A}_{mi}(z+\delta z,t)|$ and $\delta_t\mathcal{A}_{mi} := |\mathcal{A}_{mi}(z,t) - \mathcal{A}_{mi}(z,t+\delta t)|$.

http://dx.doi.org/10.5772/intechopen.72458

crosstalk among cores when assuming a single polarization. Second, we will discuss the intra- and inter-core birefringent effects by including two polarizations per core. Later, we will analyze the intermodal dispersion and its impact on Gaussian pulses and optical solitons. And finally, higher-order coupling and nonlinear effects will be investigated when propagating optical pulses in the femtosecond regime.

3.1. Inter-core crosstalk

In multi-dielectric media, we can observe mode-coupling among adjacent dielectric regions. The continuity of the electromagnetic field in such media is the physical origin of the mode-coupling, referred to as the inter-core crosstalk (IC-XT) in MCFs.

The IC-XT behavior is induced by the longitudinal and temporal deterministic and random MCF perturbations. The longitudinal perturbations include the macrobending, microbending, fiber twisting and the intrinsic manufacturing imperfections of the fiber. The temporal perturbations are induced by external environmental factors, such as temperature variations and floor vibrations modifying the propagation constant of each polarized core mode, the bending radius and the twist rate of the optical medium. In spite of the fact that the deterministic nature of the intrinsic manufacturing imperfections, the remaining perturbations present a random nature, and therefore, the IC-XT will have a stochastic evolution in the time and space domain [33, 45–50].

Figure 2 shows the temporal evolution of the IC-XT measured during 26 hours in a homogeneous 4-core MCF [Fibercore SM-4C1500(8.0/125)] between two adjacent cores in the linear and nonlinear regimes (power launch levels of 0 and 17 dBm, respectively). Although the bending radius and the twist rate present a constant value in the experimental set-up (see [49] for more details), the slight longitudinal and temporal local variations of both fiber parameters induce a longitudinal and temporal random evolution of the IC-XT in both power regimes. In addition, in the nonlinear regime, the Kerr effect is stimulated in the illuminated core 3 reducing the index-matching between the measured cores 1 and 3. In this scenario, the homogeneous cores 1 and 3 become heterogeneous when high power launch levels are injected in a

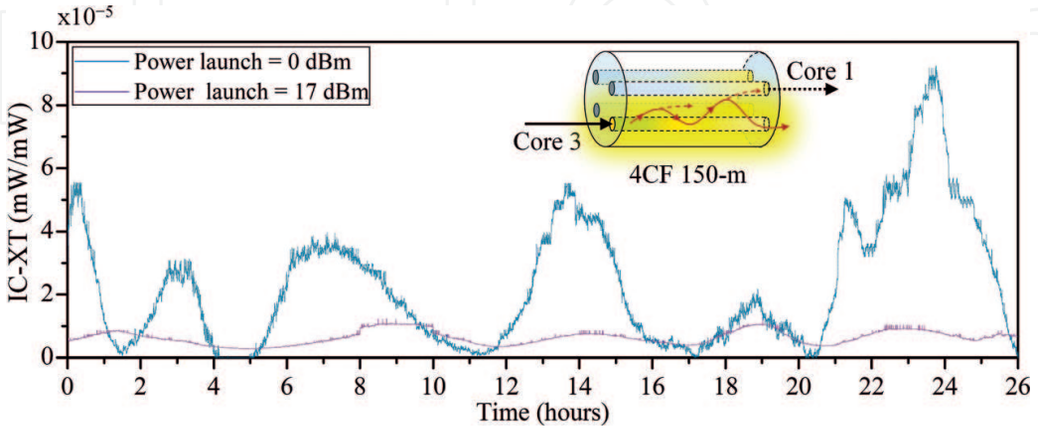

Figure 2. Measured temporal profile of the linear and nonlinear IC-XT between adjacent cores in a homogeneous 4-core MCF (results based on [49]).

given core. As a result, the MCF can be modeled in the nonlinear regime as an asymmetric optical coupler with random behavior, and consequently, the IC-XT mean and variance is reduced.

From these results, we conclude that the IC-XT has a random nature in both linear and nonlinear power regimes. Hence, at this point it is natural to ask how the probability distribution is. In a first investigation of this impairment, the answer can be easily found from the perturbation theory by assuming several initial simplifications: two cores a and b, a single polarization x and monochromatic electric fields. The last two approximations allow us to reduce the mathematical discussion of the IC-XT. In the next sections, these approximations will be revisited. Therefore, following a similar and simple approach as in the first works of the IC-XT [33, 45–50], the global electric field strength of the weakly guiding MCF (only two cores a and b and a single polarization x) is expressed as:

$$\begin{aligned}\mathcal{E}(\boldsymbol{r},t) &\approx \sum_{m=a,\,b}\mathcal{E}_m(\boldsymbol{r},t)\hat{x} \approx \sum_{m=a,\,b}\mathrm{Re}\left[E_{m,\,\omega_0}(\boldsymbol{r})\exp(j\omega_0 t)\right]\hat{x}\\ &= \sum_{m=a,\,b}\mathrm{Re}\left[A_m(z)F_m(x,y,\omega_0)\exp\left(-j\beta_m(\omega_0)z\right)\exp(j\omega_0 t)\right]\hat{x},\end{aligned} \tag{2}$$

where A_m is the complex envelope[11] of the continuous wave in the core $m = a,b$ satisfying the SVEA; F_m is the transversal eigenfunction of the LP_{01} mode in the core m; and β_m is the phase constant at the angular frequency ω_0 of the optical carrier. Note that the eigenmodes are written in Eq. (2) assuming isolated cores. Nonetheless, as mentioned before, A_m should be assumed z-dependent to model the longitudinal variations induced by the IC-XT in the core modes. Moreover, it can be noted that the MCF perturbations have been omitted in our ansatz (first step of **Figure 1**). In these previous works [33, 45–50], the MCF perturbations will be inserted heuristically[12] in the fourth step with fortunate final results. Now, using Eq. (2) in the MMEs and following the steps detailed in **Figure 1** omitting the MCF perturbations, we obtain the coupled equations of the classical coupled-mode theory (CMT) of an asymmetric and nonlinear optical coupler:

$$j\frac{\mathrm{d}A_a(z)}{\mathrm{d}z} = k_{ab}\exp\left(-j\Delta\beta_{ba}z\right)A_b(z) + q_{1a}|A_a(z)|^2A_a(z), \tag{3}$$

and a similar expression is found for $\mathrm{d}A_b(z)/\mathrm{d}z$. In Eq. (3), k_{ab} is the linear coupling coefficient, q_{1a} is the self-coupling nonlinear coefficient and $\Delta\beta_{ba} := \beta_b(\omega_0) - \beta_a(\omega_0)$. In general, additional linear and nonlinear coupling coefficients appear in Eq. (3) [50]. However, considering that the core pitch is usually higher than four times de core radius in CC- and UC-MCFs, these

[11] Note that in Eq. (2) we have employed a different function for the complex envelope as in Eq. (1). We will use $\mathcal{A}(z,t)$ to describe the complex envelope in the non-monochromatic regime (optical pulses) and $A(z)$ in the monochromatic regime (continuous waves). Both functions are related as indicated in Section 3.3.

[12] This strategy is mathematically questionable. Note that the propagation constants are assumed invariant in the ansatz [Eq. (2)], but once we derive the coupled equations, we will assume that the MCF perturbations modify the propagation constants. Although the final estimation of the IC-XT is in line with the experimental results in [47-51], in Section 3.2 we will solve this mathematical inconsistence.

coupling coefficients can be neglected [50]. The predominant coupling coefficients describe the linear and nonlinear mode-coupling: k_{ab} models the linear mode overlapping between the transversal eigenfunctions F_a and F_b, and q_{1a} allows us to investigate the self-coupling effect in the nonlinear regime (analog to the self-phase modulation which can be observed when propagating optical pulses in a single-core fiber). At this point, the MCF perturbations can be described by modifying heuristically the exponential term in Eq. (3) as follows:

$$\exp(-j\Delta\beta_{ba}z) \rightarrow \exp(-j\Delta\phi_{ba}(z)) = \exp\left(-j\int_0^z \Delta\beta_{ba}^{(\mathrm{eq})}(\tau)\mathrm{d}\tau\right), \tag{4}$$

with $\Delta\beta_{ba}{}^{(\mathrm{eq})}(z) = \Delta\beta_{ba} + \Delta\beta_{ba}{}^{(\mathrm{B}+\mathrm{S})}(z)$, where $\Delta\beta_{ba}{}^{(\mathrm{B}+\mathrm{S})}$ describes the phase fluctuation induced by the MCF perturbations. As can be seen, the temporal fluctuations of the propagation constants are also omitted in Eq. (4) to simplify the first analysis of the IC-XT. The temporal fluctuations of the crosstalk will be discussed later. Hence, the coupled-mode equation in a real MCF is finally found as:

$$j\frac{\mathrm{d}A_a(z)}{\mathrm{d}z} = k_{ab}\exp(-j\Delta\phi_{ba}(z))A_b(z) + q_{1a}|A_a(z)|^2A_a(z). \tag{5}$$

Remarkably, the revisited CMT constitutes a fundamental tool to estimate numerically the IC-XT in SM-MCFs using the Monte Carlo method [50]. The numerical calculation can also be performed in HA- and TA-MCFs by using Eq. (5) along with the corresponding closed-form expression of the linear coupling coefficient k_{ab} detailed in [51]. Furthermore, the revisited CMT allows us to derive the closed-form expressions of the IC-XT cumulative distribution function (cdf), probability density function (pdf), mean and variance in the linear and nonlinear regimes. Although the details of the mathematical discussion can be found in [33] for the linear regime and in [50] for the nonlinear regime, let us summarize the main results of these works.

The starting point is to consider a constant or quasi-constant bending and twisting conditions, i.e. their average value much higher than their longitudinal random fluctuations. In such a case, the phase-mismatching function of Eq. (4) can be expressed as [52]:

$$\Delta\phi_{ba}(z) \approx \Delta\beta_{ba}z - \frac{\beta_a d_{ab}}{2\pi f_{\mathrm{T}}(z)R_{\mathrm{B}}(z)}\sin\left(2\pi f_{\mathrm{T}}(z)z\right), \tag{6}$$

where $R_{\mathrm{B}}(z)$ and $f_{\mathrm{T}}(z)$ are the bending radius and the twist rate along the MCF length, respectively[13]. The previous expression is the same as Eq. (2) of [52], but assuming to be null the offset of the twist angle of the core a at $z = 0$. It should be noted that the power exchanged between the cores a and b is maximized at the z-points where phase-mismatching function becomes null. These points are referred to as the phase-matching points (denoted as N_{L} and N_{NL} in the linear

[13] Eq. (6) is valid if and only if we can assume that $R_{\mathrm{B}} >> \delta R_{\mathrm{B}}$ and $f_{\mathrm{T}} >> \delta f_{\mathrm{T}}$ along the MCF length. In other case, Eq. (4) must be solved numerically using the refractive index model of [33].

and nonlinear regime, respectively). In general, in homogeneous SM-MCFs $N_{L(NL)} \neq 0$, but in the heterogeneous case, the phase-matching points can only be observed for a bending radius with an average value[14] R_B lower than the threshold R_{pk} (phase-matching region[15]) [33]:

$$R_B < R_{pk} = d_{ab}\beta_a / \left|\Delta\beta_{ba}\right|. \quad (7)$$

In the phase-matching region, we can use a first-order solution of Eq. (5) to perform the statistical analysis of the IC-XT [33, 50]. **Table 2** shows the analytical expressions of the linear and nonlinear IC-XT distribution and its statistical parameters derived from the CMT. As can be seen, the measured IC-XT pdf fits correctly to a chi-squared distribution with 4 degrees of freedom. In the linear regime, the mean, variance and N_L are constant with the optical power launch level (P_L). However, in the nonlinear regime, the Kerr effect detunes the phase constant of the core modes as P_L increases in the excited core 3 and, therefore, the homogeneous MCF becomes heterogeneous. As a result, the statistical IC-XT parameters are reduced with $P_L > 2$ dBm, the critical optical power in silica MCFs [49].

Furthermore, note that these statistical parameters can be estimated from the mean of the linear crosstalk $\mu_{L,ab}$. Hayashi, Koshiba and co-workers reported in [47, 48] the closed-form expressions to estimate $\mu_{L,ab}$ in different MCF designs with different bending twisting conditions. For small bending radius with $R_B < R_{pk}$, $\mu_{L,ab}$ can be estimated using Eq. (27) of [48], and for large bending radius with $R_B > R_{pk}$, $\mu_{L,ab}$ can be estimated from Eq. (21)[16] of [47]. In **Table 2** we also include the evolution of $\mu_{L,ab}$ with the average value of the bending radius in a heterogeneous SM-MCF [47]. In the phase-matching region, the mean of the linear IC-XT increases with R_B. However, in the phase-mismatching region, the mean of the linear IC-XT is reduced when R_B increases.

Finally, it should be noted that the statistical analysis previously described is only focused on the random longitudinal evolution of the IC-XT along the MCF considering a single polarization and temporal invariant conditions of the optical medium[17]. Hence, the following natural step is to consider temporal varying conditions of the dielectric medium and two polarizations per core.

3.2. Birefringent effects

Now, let us assume a 2-core SM-MCF operating in the monochromatic regime as in the previous section, but considering two polarizations per core and both longitudinal and time-varying random perturbations. These initial assumptions will allow us to predict the different

[14] In the following equations, we denote the average value of the bending radius and the twist rate without the usual brackets < > to simplify the mathematical expressions, that is, $R_B(z) \equiv R_B + \delta R_B(z)$ and $f_T(z) = f_T + \delta f_T(z)$.

[15] Note that $R_{pk} = \infty$ when considering homogeneous cores.

[16] In [48], Eq. (21) is given as a function of the correlation length of MCF structural fluctuations. The MCF structural fluctuations are all the medium perturbations except the macrobends. Microbends, fiber twisting or floor vibrations are specific examples of the MCF structural fluctuations.

[17] That is, the electrical permittivity is assumed to be temporally invariant.

IC-XT	Equations	Figure/Comments
Probability density function (pdf)	$f_X(x) \approx \frac{(16L^2 q_{1a}^2 P_L^2 x^3 + 4x)}{N_{NL}^2 \lvert K_{ab}\rvert^4} \times \exp\left(-\frac{L^2 q_{1a}^2 P_L^2 x^3 + x}{N_{NL}\lvert K_{ab}\rvert^2/2}\right) u(x)$	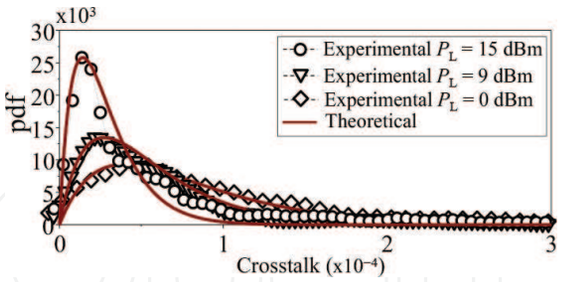
Mean	$\mu_{NL,ab} \approx \frac{\mu_{L,ab}}{1+bLP_L}$ $\mu_{L,ab} \approx \frac{2k_{ab}^2 R_B L}{\sqrt{\left(\frac{\beta_a d_{ab}}{R_B}\right)^2 - \Delta\beta_{ba}^2}}; R_B < R_{pk}$ $\mu_{L,ab} \approx \frac{2k_{ab}^2 l_c L}{1+(\Delta\beta_{ba} l_c)^2}; \quad R_B > R_{pk}$	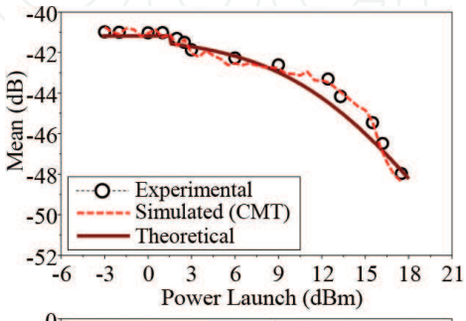 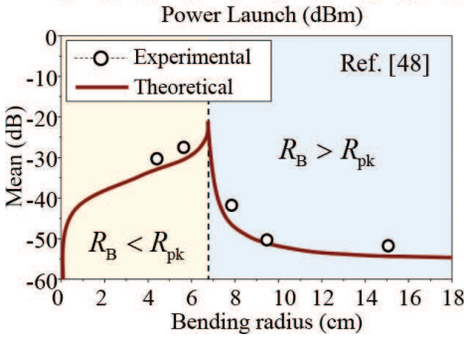
Variance	$\sigma_{NL,ab}^2 \approx \frac{\mu_{NL,ab}^2}{2} \equiv \frac{\sigma_{L,ab}^2}{(1+bLP_L)^2}$	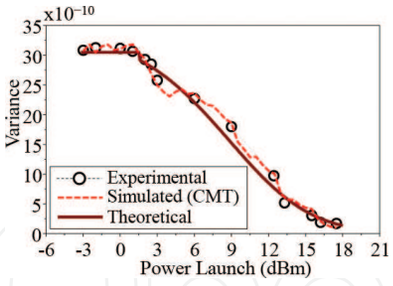
Phase-matching points	$N_{NL} \approx \frac{\mu_{NL,ab}}{\lvert K_{ab}\rvert^2} \equiv \frac{N_L}{1+bLP_L}$	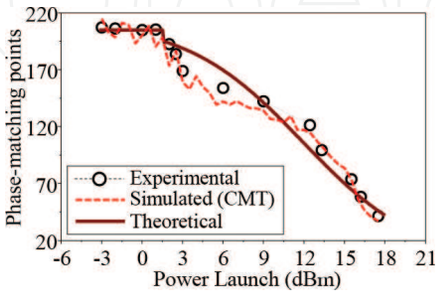

Table 2. Statistical distribution and parameters of the linear and nonlinear IC-XT. L is the MCF length, u is the Heaviside step function, P_L is the power launch level in the excited core b, K_{ab} is the discrete coupling coefficient calculated from Eq. (12) of [33], q_{1a} is the nonlinear coupling coefficient, b is a constant which depends on additional MCF parameters [50] [b = 0.5 in the Fibercore SM-4C1500(8.0/125)] and l_c is the correlation length of the autocorrelation function of the MCF structural fluctuations [47].

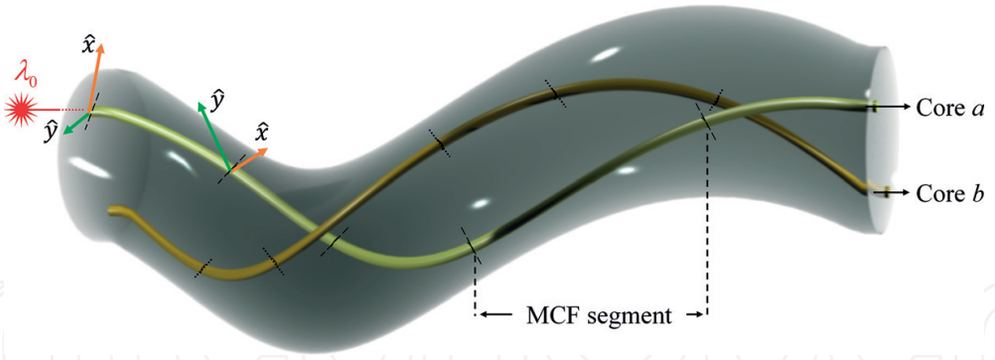

Figure 3. MCF comprising different birefringent segments in cores *a* and *b* with longitudinal and temporal varying fluctuations in the first-order electrical permittivity tensor.

crosstalk types between the polarized core modes (PCMs) in a SM-MCF: (i) the intra-core crosstalk (iC-XT) which describes the mode-coupling between orthogonal polarizations in a given core; (ii) the direct inter-core crosstalk (DIC-XT) modeling the mode coupling between the same polarization axis in different cores; and (iii) the cross inter-core crosstalk (XIC-XT) involving mode coupling between orthogonal polarizations in different cores.

As depicted in **Figure 3**, in a real MCF, each core $m = a,b$ can be modeled as a series of birefringent segments with a different time-varying retardation and random orientation of the local principal axes. Therefore, the first-order electrical susceptibility tensor $\chi_{ij}^{(1)}(\boldsymbol{r};t)$ will have both spatial and temporal dependence. As a result, in each segment of a given core m, the propagation constant of the polarized core modes (PCMs) LP_{01x} and LP_{01y} presents a different value due to the mentioned slight changes of $\chi_{ij}^{(1)}$, and therefore, the transversal function $F_{\underline{mi}}$ of each PCM "mi" ($i = x,y$) is also found to be spatial and temporal dependent.

In order to model theoretically this scenario, the concept of local mode is included in the perturbation theory. A local mode can be defined as an eigenfunction in a short core segment where the equivalent phase constant $\beta_{mi}^{(eq)}$ and the transversal function F_{mi} are approximately invariant. Hence, each core can be separated in different segments and local modes where the longitudinal and temporal birefringence conditions are approximately constant. In this way, in contrast with the previous section, now the MCF perturbations are considered from the ansatz inserted in the Maxwell equations. Specifically, the ansatz of the global electric field strength of the MCF structure is now written as [53]:

$$\begin{aligned}\mathcal{E}(\boldsymbol{r},t) &\approx \sum_{m=a,b}\sum_{i=x,y}\mathcal{E}_{mi}(\boldsymbol{r},t)\hat{u}_i \approx \sum_{m=a,b}\sum_{i=x,y}\mathrm{Re}\left[E_{mi,\omega_0}(\boldsymbol{r};t)\exp(j\omega_0 t)\right]\hat{u}_i \\ &= \sum_{m=a,b}\sum_{i=x,y}\mathrm{Re}\left[A_{mi}(z;t)F_{mi}(x,y,\omega_0;z,t)\exp(-j\Phi_{mi}(z,\omega_0;t))\exp(j\omega_0 t)\right]\hat{u}_i,\end{aligned} \tag{8}$$

where the semicolon symbol is used to separate explicitly longitudinal and temporal changes induced by the slowly varying MCF perturbations. Thus, note that the complex amplitude $E_{mi,\omega 0}$ is only a phasor with temporal changes much lower than the temporal oscillation of the optical carrier ($T_0 = 2\pi/\omega_0$). The MCF perturbations and the optical attenuation are described by the complex phase function Φ_{mi} defined as:

$$\begin{aligned}\Phi_{mi}(z,\omega_0;t) &:= \phi_{mi}(z,\omega_0;t) - j\frac{1}{2}\alpha(\omega_0)z = \int_0^z \beta_{mi}^{(\mathrm{eq})}(\delta,\omega_0;t)\mathrm{d}\delta - j\frac{1}{2}\alpha(\omega_0)z \\ &= \beta_{mi}(\omega_0)z + \int_0^z \beta_{mi}^{(\mathrm{B+S})}(\delta,\omega_0;t)\mathrm{d}\delta - j\frac{1}{2}\alpha(\omega_0)z,\end{aligned} \tag{9}$$

with α modeling the power attenuation coefficient of the MCF (assumed similar in each PCM), and the real phase function ϕ_{mi} involving the ideal phase constant of the PCM and the longitudinal and temporal MCF perturbations. Now, using Eq. (8) and performing the derivation of the perturbation theory as depicted in **Figure 1**, the following coupled local-mode equation is found [53]:

$$\begin{aligned}j\left(\frac{\partial}{\partial z}+\frac{\alpha}{2}\right)A_{ax}(z;t) &= m_{ax,ay}(z;t)\exp\left(-j\Delta\phi_{ay,ax}(z;t)\right)A_{ay}(z;t) \\ &+ k_{ax,bx}(z;t)\exp\left(-j\Delta\phi_{bx,ax}(z;t)\right)A_{bx}(z;t) \\ &+ \left(q_{ax}(z;t)\left|A_{ax}(z;t)\right|^2 + g_{ax}(z;t)\left|A_{ay}(z;t)\right|^2\right)A_{ax}(z;t) \\ &+ \frac{1}{2}g_{ax}(z;t)\exp\left(-j2\Delta\phi_{ay,ax}(z;t)\right)A_{ax}^*(z;t)A_{ay}^2(z;t),\end{aligned} \tag{10}$$

where $m_{ax,ay}$, $k_{ax,bx}$, q_{ax} and g_{ax} are the coupling coefficients defined in [53]; and the phase-mismatching functions are defined as $\Delta\phi_{ay,ax} := \phi_{ay} - \phi_{ax}$, $\Delta\phi_{bx,ax} := \phi_{bx} - \phi_{ax}$ and $\Delta\phi_{by,ax} := \phi_{by} - \phi_{ax}$. From the above equation, the following considerations are in order:

- In contrast with the previous section, the longitudinal and temporal MCF perturbations are now modeled, not only by the phase-mismatching functions $\Delta\phi(z;t)$, but also by space- and time-varying coupling coefficients[18]. This coupled local-mode theory (CLMT) inherently incorporates these stochastic perturbations in both functions, as they were directly included in the Maxwell equations using Eq. (8).
- The CLMT is completed by three additional coupled local-mode equations for the *ay*, *bx* and *by* PCMs, which can be obtained just by exchanging the corresponding subindexes in Eq. (10). The herein presented theory is a general model which can be applied to SM-MCFs comprising: coupled or uncoupled cores, lowly or highly birefringent cores, trench-assisted, hole-assisted, and with gradual-index or step-index profile. In SM-CC-MCFs with a core pitch value (d_{ab}) lower than three times the maximum core radius (R_0 = max $\{R_{0a}, R_{0b}\}$), additional nonlinear terms modeling cross-coupling effects should be included in Eq. (10). However, if we assume a MCF with $d_{ab} >> 3R_0$, the self-coupling effect is the predominant nonlinear coupling effect and the additional nonlinear terms can be neglected [53].

[18] Note that the explicit dependence with ω_0 has been omitted in the phase-mismatching functions and in the coupling coefficients for the sake of simplicity.

- The monochromatic equivalent refractive index model (ERIM) reported in [53] must be used to calculate numerically the coupling coefficients and the phase-mismatching functions. Thanks to the CLMT and the ERIM, we will observe that the temporal birefringence fluctuation of each core modifies the average value of the iC-, DIC- and XIC-XT.

First, in order to analyze the longitudinal MCF random perturbations induced by MCF bending and twisting, a Monte Carlo simulation was performed using the CLMT along with the ERIM considering a 2-m SI-SM-HO-UC-LB-2CF with cores *a* and *b* comprising a single birefringent segment with the same birefringence average value of $<\Delta n_{aj}> = <\Delta n_{bj}> = 10^{-7}$ (see the specific fiber parameters in [53]). The temporal birefringence fluctuation of the 2CF was omitted in this simulation. The numerical results are shown in **Figure 4**, where we can observe the behavior of the mean of the iC-XT *ay-ax* DIC-XT *bx-ax* and XIC-XT *by-ax* when changing the bending radius R_B and fiber twisting conditions f_T.

As it can be noticed from **Figure 4(a)**, we cannot observe intra-core mode-coupling between *ax-ay* with $f_T = 0$ in 2 m of the MCF. Macrobending increases the phase-mismatching between the PCMs *ax* and *ay* without inducing iC-XT due to the photo-elastic effect [54]. As a result, significant XIC-XT cannot be observed for short MCF lengths when $f_T = 0$, as in the case of **Figure 4(c)**. Nevertheless, an average level of DIC-XT between −100 and −50 dB can be noted from **Figure 4(b)** in non-twisting conditions depending on the R_B value. In addition, the higher the twist rate and the bending radius, the higher the iC-, DIC- and XIC-XT mean due to the reduction of the phase-mismatching between the different PCMs of the 2CF. Note that DIC- and XIC-XT means are balanced when the iC-XT mean achieves the value of 0 dB in **Figure 4(a)**. Therefore, MCF twisting can be proposed as a potential strategy for birefringence management to balance the inter-core crosstalk between the different PCMs for short MCF distances. For MCF distances of several kilometers, the iC-XT mean will be increased and the difference between the mean of the DIC- and XIC-XT will be reduced.

In addition, experimental measurements were performed on a 4CF [Fibercore SM-4C1500 (8.0/125)] analyzing the temporal birefringence of the optical media and its impact on the mean of the crosstalk between the PCMs of the cores 1 and 3. **Figure 5** shows the temporal fluctuation of the linear birefringence and the crosstalk mean behavior between the PCMs of cores 1

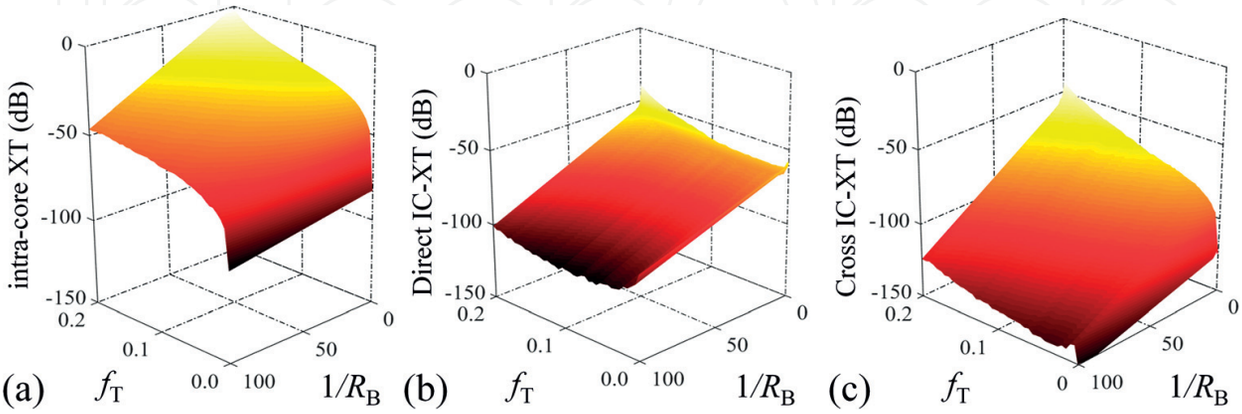

Figure 4. Numerical simulation of the crosstalk between PCMs varying the bending radius and the twist rate in a 2-m SI-SM-HO-UC-LB-2CF: (a) iC-XT mean *ay-ax*, (b) DIC-XT mean *bx-ax*, and (c) XIC-XT mean *by-ax*.

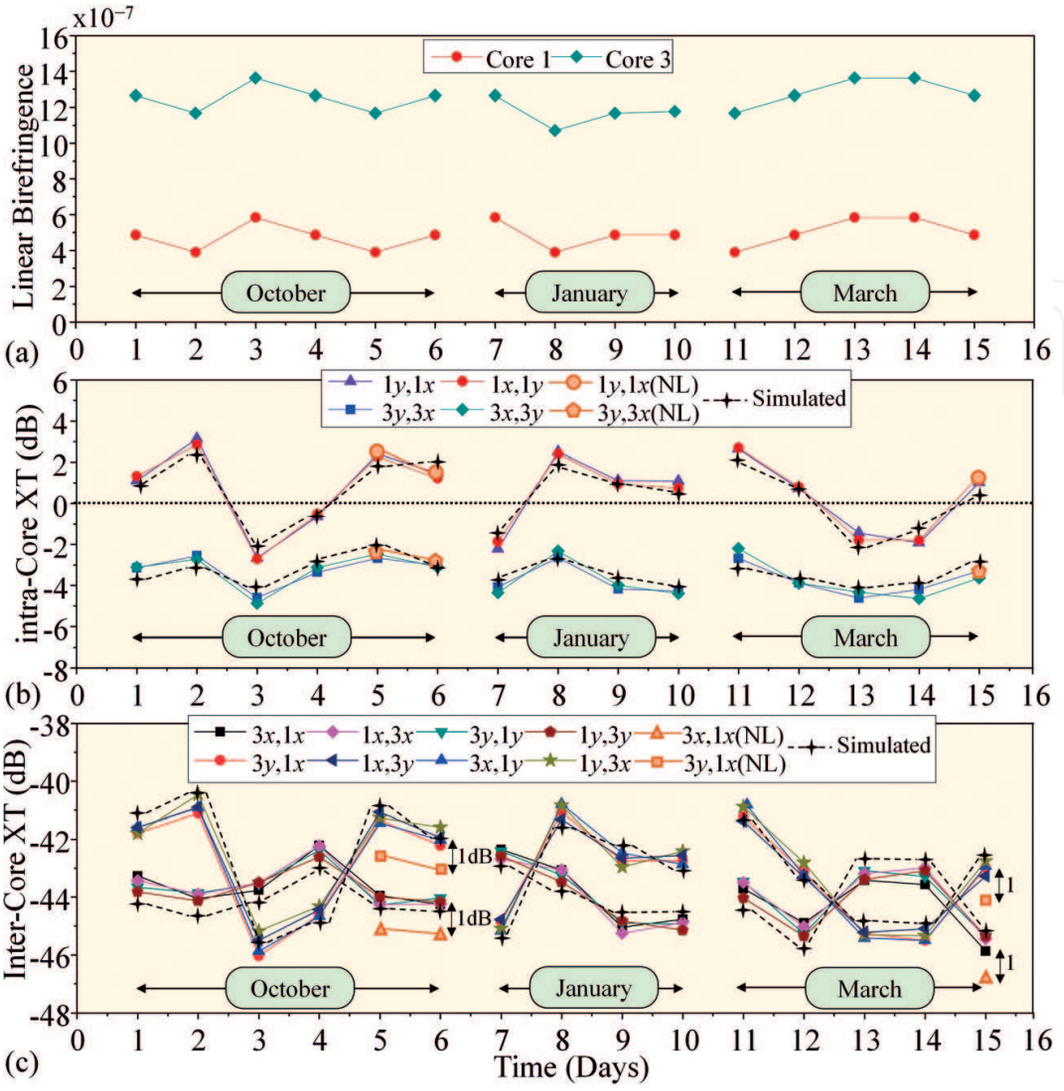

Figure 5. Experimental results of the temporal linear birefringence fluctuation over different days and months of a 150-m 4CF, and corresponding intra- and inter-core crosstalk mean between cores 1 and 3 (NL: nonlinear regime). (a) Linear birefringence of the cores 1 and 3, (b) iC-XT and (c) DIC- and XIC-XT. Results based on [53].

and 3 measured in different days and months[19]. As shown in **Figure 5(a)**, cores 1 and 3 present a different average value of the linear birefringence estimated to be $\langle \Delta n_{1,j} \rangle = 4.9 \cdot 10^{-7}$ and $\langle \Delta n_{3,j} \rangle = 1.2 \cdot 10^{-6}$, respectively ($j = 1,\ldots,15$). It can be noted that the average value of the linear birefringence is found to be constant in each core the three different measured months. Moreover, although the average value of the linear birefringence is different in each core, the temporal evolution of the linear birefringence presents a similar shape in both cores. As can be seen from **Figure 5(a)** and **(b)**, the higher the linear birefringence in a given core, the lower the mean of the iC-XT. Furthermore, it should be noted that iC-XT in core 3 is lower than in core 1 due to a higher index-mismatching between the orthogonal polarizations. Remarkably,

[19] As the linear birefringence of each core remains unchanged during more than 10 hours in the laboratory room, we analyzed the temporal birefringence fluctuation in different days and months, with similar temperature conditions in the laboratory.

the iC-XT mean presents a lower temporal fluctuation in the more birefringent core (core 3), which occurs when the average value of the birefringence is higher than the temporal random birefringence fluctuation (~10^{-7}). In addition, we can observe from **Figure 5(c)** that the temporal evolution of the XIC-XT mean presents the same behavior as the iC-XT mean, indicating that XIC-XT depends directly on the iC-XT of both cores. As a result, DIC-XT is higher than XIC-XT when iC-XT is lower than 0 dB in both cores. The nonlinear crosstalk between de PCMs 1*y*-1*x*, 3*y*-3*x*, 3*x*-1*x* and 3*y*-1*x* was also measured the 5th, 6th and 15th days with a power launch level of 6 dBm. The DIC- and XIC-XT mean is reduced around 1 dB keeping constant the difference between both inter-core crosstalk types as a direct consequence of the constant behavior of the iC-XT mean in nonlinear regime. Finally, note that the experimental measurements of **Figure 5** fit correctly with the CLMT when using the simulation parameters detailed in [53].

Additional numerical calculations of the CLMT can be found in [53] involving both LB and HB cores. Interesting, it is worth mentioning that the CLMT and the ERIM can be used to design HB-MCFs with random orientation of the principal axes between adjacent cores to reduce the mode-coupling between their PCMs. The concept is similar to the crosstalk behavior which can be found in disordered MCFs exhibiting transverse Anderson localization [21]. Along this line, a TA- and HA-cladding can also be considered in these fibers to obtain low DIC- and XIC-XT levels. In all these scenarios, the CLMT can be used in the design work, with a lower computational time than numerical simulations based on FDTD (Finite-Difference Time Domain) calculations.

The temporal fluctuation of the crosstalk has also been investigated in [55], but considering a single polarization per core and inserting heuristically the MCF perturbations in the exponential terms of the CMT, in line with the initial crosstalk works [33, 45–50]. Specifically, in ref. [55], the crosstalk transfer function has been discussed at the MCF output considering small modulated signals, i.e. non-monochromatic electric fields. However, the comprehension of the MCF propagation and the IC-XT in the non-monochromatic regime is not as straightforward as initially foreseen. Hence, at this point, let us discuss the non-monochromatic regime with a similar rigorous formalism as in [53] for the monochromatic case.

3.3. Intermodal dispersion and higher-order coupling and nonlinear effects

The theoretical study of the non-monochromatic regime will allow us to describe the propagation of optical pulses through a MCF. Focusing our efforts on SM-MCFs, additional physical impairments should be included in Eq. (10), such as the group-velocity dispersion (GVD), polarization-mode dispersion (PMD), intermodal dispersion and additional nonlinear effects. Moreover, if we also consider the propagation of ultra-short optical pulses in the femtosecond regime, the analysis of higher-order coupling and nonlinear effects should also be incorporated to the coupled equations.

Although in the picosecond regime MCF propagation models have been proposed in [56, 57] including polarization effects and the random longitudinal fiber perturbations (but omitting the temporal fluctuations), in the femtosecond regime, existing MCF propagation models exclude polarization effects and omit both temporal and longitudinal random perturbations

of the fiber [58–60]. In order to include these realistic fiber conditions in the mathematical description of the propagation of femtosecond optical pulses through a MCF, a theoretical model is proposed in [61] based on the concept of local modes. As can be seen later, the intermodal dispersion induced by the MCF random perturbations can become one of the major physical impairment in the single-mode regime of the fiber. Specifically, the intermodal dispersion, also referred to as the mode-coupling dispersion (MCD) in this work, is induced in the femtosecond regime not only by the mismatching between the propagation constants of the PCMs, but also by the frequency dependence of their mode overlapping.

Our initial goal is to revisit the CLMT of the previous section but now assuming non-monochromatic fields. In such a case, the ansatz of the global electric field strength of a SM-MCF should be written as:

$$\mathcal{E}(\boldsymbol{r},t) \approx \sum_{m=a,\,b} \sum_{i=x,\,y} \mathcal{E}_{mi}(\boldsymbol{r},t)\hat{u}_i \approx \sum_{m=a,\,b} \sum_{i=x,\,y} \mathrm{Re}\left[E_{mi,\,\omega_0}(\boldsymbol{r},t)\exp(j\omega_0 t)\right]\hat{u}_i, \tag{11}$$

where the complex amplitude $E_{mi,\omega 0}$ is now a bandpass signal with the slowly varying temporal changes of the electric field strength, given by the expression:

$$\begin{aligned} E_{mi,\,\omega_0}(\boldsymbol{r},t) = \frac{1}{2\pi}\int \tilde{A}_{mi}(z,\omega-\omega_0;t)F_{mi}(x,y,\omega;z,t)\times \\ \times \exp[-j\Phi_{mi}(z,\omega;t)]\exp[j(\omega-\omega_0)t]\mathrm{d}\omega. \end{aligned} \tag{12}$$

The functions involved in the previous equations are the same as in Eq. (8), but now expressed in the frequency domain. Nevertheless, a fundamental remark of the complex envelope should be taken into account at this point. As previously discussed in **Figure 1**, the slowly varying longitudinal changes should also be decoupled from the rapidly varying longitudinal fluctuations via the complex envelope. However, in Eq. (12) the rapidly and slowly varying longitudinal changes are coupled in the first exponential term via the function $\phi_{mi}(z,\omega;t)$. Therefore, in order to decouple them and model the analytic function of the optical pulses, the complex envelope should be rewritten as:

$$\tilde{\mathcal{A}}_{mi}(z,\omega-\omega_0;t) = \tilde{A}_{mi}(z,\omega-\omega_0;t)\exp[-j(\phi_{mi}(z,\omega;t)-\phi_{mi}(z,\omega_0;t))]. \tag{13}$$

Once we have written our ansatz of the global electric field strength, the following step is to propose the wave equation of the PCMs (second step) and the wave equation of the MCF (third step). In particular, in the third step, we will able to incorporate the higher-order nonlinear effects via the constitutive relation between the global electric field strength and the nonlinear polarization. Note that in the femtosecond regime, the aforementioned constitutive relation should include the delay response of the electronic and nuclei structure of silica atoms [62]. For optical frequencies well below the electronic transitions, the electronic contribution to the nonlinear polarization can be considered instantaneous. However, since nucleons (protons and neutrons) are considerably heavier than electrons, the nuclei motions have resonant frequencies much lower than the electronic resonances and, consequently, they should be retained in the constitutive relation as indicated in Eq. (S36) of [61]. Specifically, Raman

scattering is a well-known effect arising from the nuclear contribution to the nonlinear polarization. All in all, the coupled local-mode equations can be derived to describe the propagation of ultra-short pulses in SM-MCFs. In particular, the coupled local-mode equation modeling the propagation of the PCM *ax* is found to be [61]:

$$\begin{aligned} j\left(\frac{\partial}{\partial z}+\widehat{\mathrm{D}}_{ax}^{(\mathrm{eq})}+\frac{1}{2}\widehat{\alpha}\right)\mathcal{A}_{ax}(z,t) &= \widehat{\mathrm{M}}_{ax,\,ay}^{(\mathrm{eq})}\mathcal{A}_{ay}(z,t)+\sum_{m=b}^{N}\widehat{\mathrm{K}}_{ax,\,mx}^{(\mathrm{eq})}\mathcal{A}_{mx}(z,t) \\ &+\widehat{\mathrm{q}}_{ax}^{(\mathrm{I})}\left(|\mathcal{A}_{ax}(z,t)|^2\mathcal{A}_{ax}(z,t)\right)+\frac{2}{3}\widehat{\mathrm{g}}_{ax,\,ay}^{(\mathrm{I})}\left(\left|\mathcal{A}_{ay}(z,t)\right|^2\mathcal{A}_{ax}(z,t)\right) \\ &+\frac{1}{3}\exp\left(-j2\Delta\phi_{ay,\,ax}^{(0)}(z;t)\right)\widehat{\mathrm{g}}_{ax,\,ay}^{(\mathrm{I})}\left(\mathcal{A}_{ax}^{*}(z,t)\mathcal{A}_{ay}^{2}(z,t)\right) \\ &+\widehat{\mathrm{q}}_{ax}^{(\mathrm{R})}\left[\left(f(t)*|\mathcal{A}_{ax}(z,t)|^2\right)\mathcal{A}_{ax}(z,t)\right]+\widehat{\mathrm{g}}_{ax,\,ay}^{(\mathrm{R})}\left[\left(h(t)*\left|\mathcal{A}_{ay}(z,t)\right|^2\right)\mathcal{A}_{ax}(z,t)\right] \\ &+\frac{1}{2}\widehat{\mathrm{g}}_{ax,\,ay}^{(\mathrm{R})}\left\{\left[u(t)*\left(\mathcal{A}_{ax}(z,t)\mathcal{A}_{ay}^{*}(z,t)\right)\right]\mathcal{A}_{ay}(z,t)\right\} \\ &+\frac{1}{2}\exp\left(-j2\Delta\phi_{ay,\,ax}^{(0)}(z;t)\right)\widehat{\mathrm{g}}_{ax,\,ay}^{(\mathrm{R})}\left\{\left[u(t)*\left(\mathcal{A}_{ax}^{*}(z,t)\mathcal{A}_{ay}(z,t)\right)\right]\mathcal{A}_{ay}(z,t)\right\}. \end{aligned} \tag{14}$$

where $\widehat{\mathrm{D}}_{ax}^{(\mathrm{eq})}$ is the equivalent dispersion operator in the PCM *ax* including the frequency dependence of the MCF perturbations in the time domain; $\widehat{\alpha}$ is the attenuation operator; the *h* and *u* functions describe the isotropic and anisotropic Raman response, respectively; the *f* function is *f*:= *h* + *u*; the phase-mismatching term $\Delta\phi_{ay,\,ax}^{(0)}(z;t) := \phi_{ay}(z,\omega_0;t)-\phi_{ax}(z,\omega_0;t)$ describes the phase-mismatching between the PCMs *ax* and *ay* at ω_0; $\widehat{\mathrm{M}}_{ax,\,ay}^{(\mathrm{eq})}$ and $\widehat{\mathrm{K}}_{ax,\,mx}^{(\mathrm{eq})}$ are, respectively, the equivalent intra- and inter-core mode-coupling dispersion operators between the PCMs *ax-ay* and *ax-mx*; $\widehat{\mathrm{q}}_{ax}^{(\mathrm{I})}$ and $\widehat{\mathrm{g}}_{ax,\,ay}^{(\mathrm{I})}$ are the nonlinear mode-coupling dispersion operators associated with the instantaneous response of the nonlinear polarization and accounting for the nonlinear mode overlapping between the PCMs *ax-ax* and *ax-ay*; and $\widehat{\mathrm{q}}_{ax}^{(\mathrm{R})}$ and $\widehat{\mathrm{g}}_{ax,\,ay}^{(\mathrm{R})}$ are analogous to $\widehat{\mathrm{q}}_{ax}^{(\mathrm{I})}$ and $\widehat{\mathrm{g}}_{ax,\,ay}^{(\mathrm{I})}$, but associated with the nonlinear polarization induced by the delay response of the nuclei motion of silica atoms (Raman effect). A comprehensive description of the main parameters of the model can be found in [61].

It should be remarked that the linear operators of Eq. (14) are found to be longitudinal and temporal dependent, instead of constant coupling coefficients and unperturbed propagation constants. Thanks to these linear operators, Eq. (14) is able to describe accurately the linear and nonlinear propagation of each PCM and the linear and nonlinear MCD including the longitudinal and temporal MCF perturbations. Furthermore, it is worthy to note that the MCD is induced in each birefringent segment by two different dispersive effects when propagating femtosecond optical pulse through a MCF: (i) the frequency dependence of the local mismatching between the phase functions $\phi_{mi}(z,\omega;t)$ of the PCMs, referred to as the phase-mismatching dispersion (PhMD); and (ii) the frequency dependence of the mode overlapping between the PCMs, modeled by the coupling coefficients and referred to as the coupling coefficient dispersion (CCD). As an example, the PhMD between the PCMs *ax* and *mx* is given by the phase-mismatching $\Delta\phi_{mx,ax}(z,\omega;t)$ and the CCD by the coupling coefficients

$\tilde{k}_{ax,mx}(z,\omega;t)$ and $\tilde{k}_{mx,ax}(z,\omega;t)$, both dispersive effects modeled by the operators $\widehat{\mathrm{D}}_{ax}^{(\mathrm{eq})}$, $\widehat{\mathrm{D}}_{mx}^{(\mathrm{eq})}$, $\widehat{\mathrm{K}}_{ax,mx}^{(\mathrm{eq})}$ and $\widehat{\mathrm{K}}_{mx,ax}^{(\mathrm{eq})}$. Note that the equivalent dispersion operators $\widehat{\mathrm{D}}_{ax}^{(\mathrm{eq})}$ and $\widehat{\mathrm{D}}_{mx}^{(\mathrm{eq})}$ describe not only the linear propagation of the PCMs *ax* and *mx*, but also the exact phase-mismatching $\Delta\phi_{mx,ax}(z,\omega;t)$ at each angular frequency ω at a given z point. The MCD can be observed in a SM-MCF between the PCMs of different cores (inter-core MCD) and between the PCMs of a single core (intra-core MCD). Note that the intra-core MCD is the well-known linear and nonlinear polarization-mode dispersion (PMD). Hence, we will discuss in this subsection the inter-core MCD (IMCD) involving the mode-coupling between the PCMs of different cores.

Although the proposed model allows us to investigate a wide range of propagation phenomena in MCFs, our efforts are mainly focused on a deeper understanding of the IMCD induced by the fiber perturbations. In order to clarify the impact of the MCF birefringence on this physical impairment when propagating femtosecond optical pulses, Eq. (16) is solved numerically in the linear and nonlinear regime of the fiber. In all the analyzed cases, we considered a MCF comprising a fiber length of L = 40 m and two cores *a* and *b* distributed in a square lattice as in the Fibercore SM 4C1500(8.0/125) but with a core-to-core distance d_{ab} = 26 μm. The wavelength of the optical carrier λ_0 was selected to be in the third transmission window with λ_0 = 1550 nm. The time variable was normalized using the group delay of the PCM *ax* as a reference with $t_{\mathrm{N}} = (t - \beta_{ax}{}^{(1)}z)/T_{\mathrm{P}}$, where T_{P} is defined in this work as the full width at 1/2*e* (~18%) of the peak power.

As a first simple example, we considered an ideal homogeneous MCF, with $R_{\mathrm{B}} = \infty$ and $f_{\mathrm{T}} = 0$ turns/m. **Figure 6(a)** shows the simulation results of the CLMT when a 350-fs Gaussian optical pulse is launched into the PCM *ax* at $z = 0$. In this example, the GVD and the PMD (induced by the intrinsic random fiber birefringence) were omitted to isolate the effects of the first-order

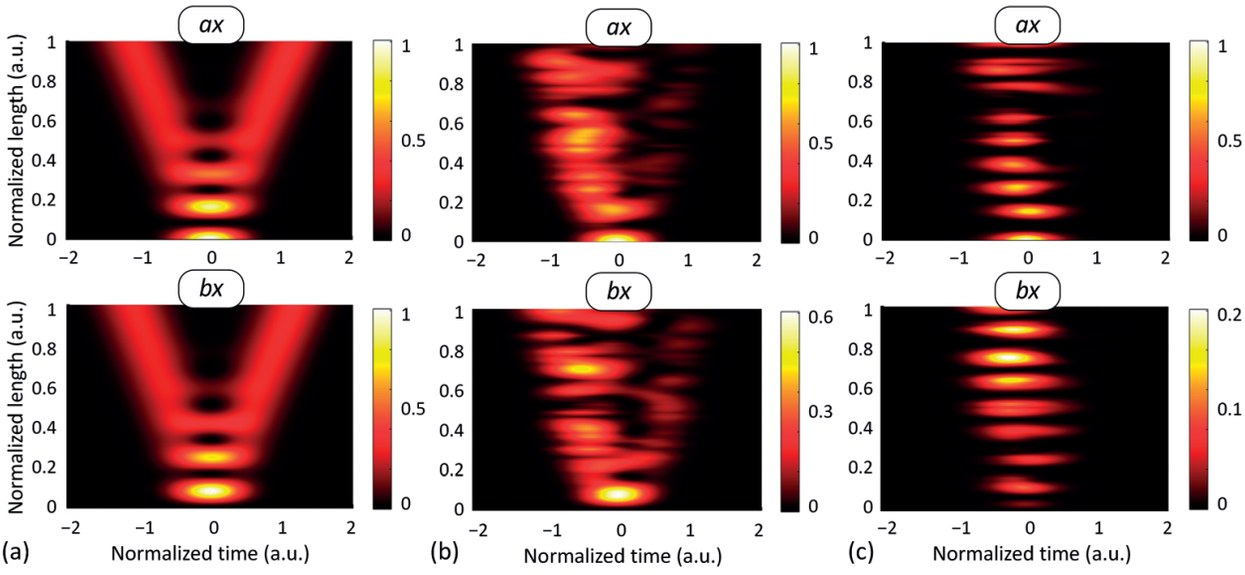

Figure 6. IMCD impact on Gaussian pulses and optical solitons propagating through a SM-MCF. (a) 350-fs Gaussian optical pulse propagation under ideal conditions. (b) 250-fs Gaussian optical pulse propagation with random bending conditions. (c) 600-fs fundamental bright soliton with random bending and twisting conditions. The numerical results for the PCMs *ay* and *by* can be found in [61].

IMCD. In this way, the pulse is only propagated by the PCMs *ax* and *bx*. Remarkably, the pulse splitting predicted by Chiang et al. in [58] appears induced by the first-order CCD: each spectral component of the pulse presents a different coupling length as a direct consequence of the linear frequency dependence of the power confinement ratio of the LP01 mode in each core. As a result, the pulse propagation can be modeled in this case by two linear and time-invariant systems with the impulse response proportional to the Dirac delta functions $\delta(t \pm Kz)$, where K is the first-order frequency derivative of the coupling coefficient between the PCMs *ax* and *bx*.

Another interesting effect of the first-order IMCD is related to the random birefringence that arises from a randomly varying fiber bending radius. In this case, the effect of the first-order PhMD along with the CCD can also be observed when considering a high number of MCF birefringent segments where the bending radius fluctuates with a Normal distribution between adjacent segments. We simulate the MCF of the first example considering a 250-fs Gaussian optical pulse and 50 birefringent segments with a bending radius Normal distribution $R_B = N(\mu = 100, \sigma^2 = 40)$ cm. The numerical results are shown in **Figure 6(b)**. It can be seen that the group delay and the pulse splitting present a random evolution in each core due to the stochastic nature of the MCF perturbations inducing a random differential group delay between the PCMs *ax* and *bx*. In particular, this result can be employed for pulse shaping and dispersion engineering applications.

In the third example, the IMCD effects are also investigated in the nonlinear fiber regime along with the PMD (intra-core MCD). Specifically, the impact of such perturbations on a bright soliton is analyzed. A 600-fs fundamental soliton (~350 fs full width at half maximum) was launched into the PCM *ax* of a dispersion-shifted homogeneous 2-core MCF with usual GVD parameters of $\beta^{(2)} = -1$ ps^2/km and $\beta^{(3)} = 0.1$ ps^3/km. The peak power (P_0) required to support the fundamental soliton is found to be around ~40 dBm considering a nonlinear refractive index of $n_{NL} = 2.6 \cdot 10^{-20}$ m^2/W at 1550 nm. In order to simulate realistic MCF conditions, we assume $\Delta\beta_{bx,ax}{}^{(1)} = 0.2$ ps/km and $\Delta\beta_{bx,ax}{}^{(2)} = 0.1$ ps^2/km induced by manufacturing imperfections (similar values for the *y*-polarization). In this case, we also include the intrinsic linear birefringence of the medium along with the linear and circular birefringence induced by the fiber bending and twisting conditions. We consider 50 birefringent segments along the MCF length, where the linear and circular birefringence fluctuate between adjacent segments. The circular birefringence is induced by a random twist rate f_T given by the Normal distribution $f_T = N(\mu = 0.1, \sigma^2 = 0.01)$ turns/m. The linear birefringence is induced by: (i) the random bending conditions with $R_B = N(\mu = 100, \sigma^2 = 40)$ cm; and (ii) the intrinsic linear birefringence of each core, fixed to $2 \cdot 10^{-7}$ in both cores *a* and *b*. According to **Figure 6(c)**, we can observe that the soliton condition is broken along the MCF propagation. The second-order PhMD becomes the main physical impairment when $\Delta\beta_{bx,ax}{}^{(2)} \neq 0$ in dispersion-shifted coupled-core MCFs, with a reduced second-order GVD coefficient and core-to-core distance. Therefore, in the first propagation meters, the additional chirp induced by the second-order PhMD along with the first-order CCD increases the pulse width and reduces the peak power. As a result of the peak power reduction, the pulse width is increased along the MCF length and the soliton peak is shifted from its original position due to the first-order PhMD and the third-order GVD. In this case, note that the effects of the Raman-induced frequency shift (RIFS) [63] and the self-

steepening are difficult to observe with $T_P = 600$ fs, $L = 40$ m, $\beta^{(2)} = -1$ ps^2/km, and $P_0 \approx 40$ dBm. Nevertheless, in optical pulses of few femtoseconds and in MCFs with a higher second-order GVD coefficient, the soliton distortion will be increased not only by the IMCD and the third-order GVD, but also by the RIFS and the self-steepening nonlinear effects.

Although we have only discussed the main effects of the longitudinal birefringence of the MCF, the analysis of the temporal perturbations of the medium can be found in [61]. It should be noted that the IMCD can also fluctuate in time due to the temporal fluctuation of the MCF birefringence modifying the value of the phase functions $\phi_{mi}(z,\omega;t)$ for the PCM mi. Therefore, the random group delay induced by the first-order PhMD in each MCF segment may present a time-varying evolution.

For completeness, we investigate the fiber length scales over which the dispersive effects of the IMCD should be considered in the pulse propagation phenomena when comparing this physical impairment with the GVD. To this end, we compare the GVD, CCD and PhMD lengths considering a MCF without random perturbations, given by the expressions for the PCMs ax and bx [61]:

$$L_{\mathrm{GVD}} := T_P^2 / \left|\beta_{ax}^{(2)}\right|; \quad L_{\mathrm{CCD}} := T_P / 2\left|\tilde{k}_{ax,bx}^{(1)}\right|; \quad L_{\mathrm{PhMD}} := T_P^2 / \left|\Delta\beta_{bx,ax}^{(2)}\right|. \tag{15}$$

Figure 7 depicts the comparison of the GVD, CCD and PhMD dispersion lengths. As can be seen, the IMCD induced by the CCD becomes the predominant impairment in dispersion-shifted coupled-core MCFs with a reduced core-to-core distance and $\Delta\beta_{bx,ax}{}^{(2)} = 0$. On the other hand, the GVD is expected to become the major physical impairment in homogeneous uncoupled-core MCFs, with a core-to-core distance d_{ab} higher than 30 μm and $\Delta\beta_{bx,ax}{}^{(2)} \approx 0$, or in heterogeneous MCFs with inter-core crosstalk levels lower than −30 dB. Nevertheless, the GVD along with the IMCD induced by the second-order PhMD will be the predominant physical impairments in homogeneous coupled-core MCFs with $\Delta\beta_{bx,ax}{}^{(2)} \neq 0$.

Finally, it should be noted that the extension of Eq. (14) to the multi-mode regime is straightforward when including additional LP mode groups in the complex amplitude of the global electric field strength $E_{i,\omega 0}$. Inserting $E_{i,\omega 0}$ in the Maxwell equations, the CLMT can be extended

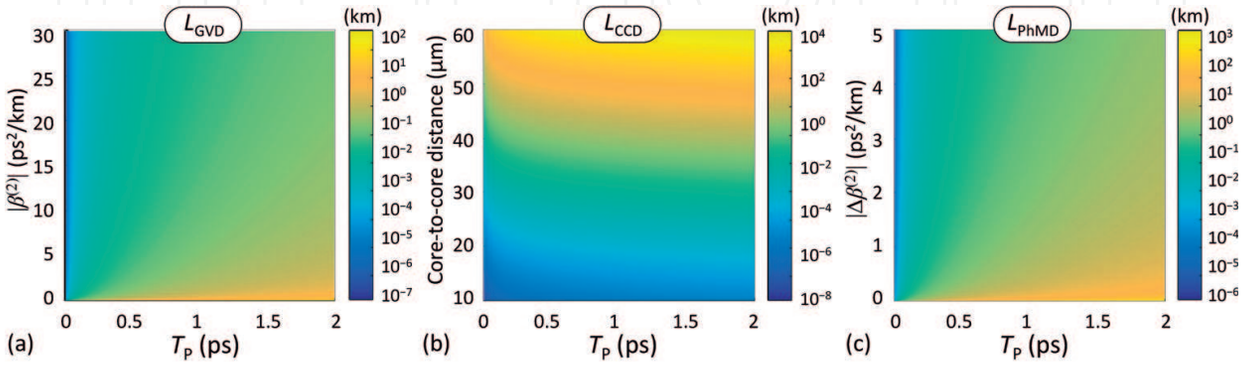

Figure 7. Comparison of the dispersion lengths. (a) Group-velocity dispersion (GVD) length, (b) coupling coefficient dispersion (CCD) length, and (c) phase-mismatching dispersion (PhMD) length.

to the multi-mode regime performing a similar mathematical discussion as in [61] in the single-mode regime.

4. Current and emerging applications

Once we have reviewed the fundamental aspects of the linear and nonlinear propagation in MCF media, we will discuss in this section the main applications and opportunities of the MCF technology in photonics and diverse branches of sciences.

4.1. Backbone and access optical networks using multi-core fibers

SDM systems using MCFs have been extensively investigated in recent years targeting to overcome the exponential growth of data traffic in the backbone and in the access network [4–7].

The first laboratory MCF transmission was demonstrated in May 2010 [64]. Zhu and co-workers used a SI-SM-HO-UC-LB-7CF with a hexagonal lattice. A novel network configuration was proposed for passive optical network (PON) based on a bidirectional parallel transmission at 1310 nm and 1490 nm and using a tapered MCF connector (TMC) for injecting and extracting the optical signals in the MCF.

A set of MCF experiments were reported since 2011. Scaling in capacity demonstrations, [65–67] should be mentioned. In [65] the authors demonstrated a 210 Tb/s self-homodyne transmission system using distributed feedback (DFB) lasers and a 19-core TA-SM-HO-UC--LB-MCF. Sakaguchi et al. reported in [66] a record capacity of 305 Tb/s over 10.1 km using the same MCF as in [65], with an IC-XT mean of −32 dB between adjacent cores at 1550 nm. The authors also fabricated a 19-channel SDM multiplexer/demultiplexer using free-space optics with low insertion losses and low additional crosstalk. As another interesting example, Takara et al. reported in [67] 1.01 Pb/s transmission over 52 km with the highest aggregate spectral efficiency of 91.4 b/s/Hz by using a one-ring-structured 12-core TA-SM-HO-UC-LB-MCF. They generated 222-channel WDM signals of 456-Gb/s PDM-32QAM-SC-FDM signals[20] with 50-GHz spacing in the C and L bands. Following significant efforts on the design and fabrication of MCFs, demonstrations of SDM transmissions using MCF media for long-haul applications have shown impressive progress in terms of capacity, reach, and spectral efficiency, as detailed in **Table 3**.

On the other hand, cloud radio-access network (C-RAN) systems should also deal with this huge future capacity demand in the next-generation wireless systems, e.g. 5G cellular technology and Beyond-5G [75–77]. According to some telecom equipment manufacturers, it is expected that 5G cellular networks will be required to provide 1000 times higher mobile data traffic in 2025 as compared with 2013, including flexibility and adaptability solutions to maximize the energy efficiency of the network [78, 79]. A new radio-access model supporting

[20]PDM: Polarization-Division Multiplexing, QAM: Quadrature Amplitude Modulation, SC: Single Carrier, FDM: Frequency-Division Multiplexing.

Year	Ref.	Fiber type	Cores × modes	Distance (km)	Channel rate (Gb/s)	WDM channels per core	S/E (b/s/Hz)	Total capacity (Tb/s)
2011	[68]	SM-MCF	7 × 1	2688	128	10	15	7
2012	[67]	SM-MCF	12 × 1	52	456	222	91.40	1012
2012	[66]	SM-MCF	19 × 1	10.1	172	100	30.50	305
2013	[65]	SM-MCF	19 × 1	10.1	100	125	33.60	210
2014	[7]	FM-MCF	7 × 2	1	4000	50	102	200
2015	[69]	SM-MCF	7 × 1	2520	100	73	16	51
2015	[70]	FM-MCF	36 × 2	5.5	107	40	108	432
2015	[71]	FM-MCF	12 × 2	527	80	20	90.28	45
2015	[72]	FM-MCF	19 × 4	9.8	40	8	345	29
2016	[73]	FM-MCF	19 × 4	9.8	60	360	456	2050
2017	[74]	SM-MCF	32 × 1	205.6	768	46	217.6	1001

Table 3. Summary of progress in MCF transmissions in recent years. The MCF type indicates only the modal regime (additional characteristics of the MCF involving the index profile, the spatial homogeneity, the core pitch and the birefringence can be found in the corresponding reference). The number of modes indicate the number of LP mode groups supported by the MCF transmission. The channel rate includes PDM and the overhead for forward-error-correction (FEC). The spectral efficiency and total capacity exclude the FEC overhead.

massive data uploading will be required considering additional transport facilities provided by the physical layer [78–80].

Fronthaul connectivity performed by radio-over-fiber (RoF) transmission using single-input single-output (SISO), multiple-input multiple-output (MIMO) configuration [81], sub-Nyquist sampling [82], and ultra-wideband signals exceeding 400 MHz bandwidth has been proposed for the 5G cellular generation [76, 77, 83]. The required channel capacity is further extended in the case of Beyond-5G systems, where a massive number of antennas operating in MIMO configuration, should be connected using RoF. To overcome the massive increment in the data capacity demand, MCF has been recently proposed as a suitable medium for LTE-Advanced (LTE-A) MIMO fronthaul systems [52, 83, 84].

MCFs open up attractive possibilities in RoF systems as different wireless signals can be transmitted simultaneously over the same optical wavelengths and electrical frequencies in different cores of the optical waveguide to provide multi-wireless service using a single laser at the transmitter. Thus, MCF can also be proposed as an alternative to the classical SM-SCF [also termed in the literature as the standard single-mode fiber (SSMF)] providing fronthaul connectivity using multiple wavelength channels with multiple lasers. Additionally, MCFs with high core density are suitable for connecting large phase array antennas performing multi-user MIMO (MU-MIMO) processing [85]. Furthermore, network operators can offer a dynamic and scalable capacity in the next cellular generation due to the aggregated channel capacity provided by the MCF technology [86]. Moreover, the possibility of combining MCF-RoF transmissions with additional multiplexing techniques such as time-division multiplexing (TDM), WDM, PDM and mode-division multiplexing (MDM) [12] should be considered.

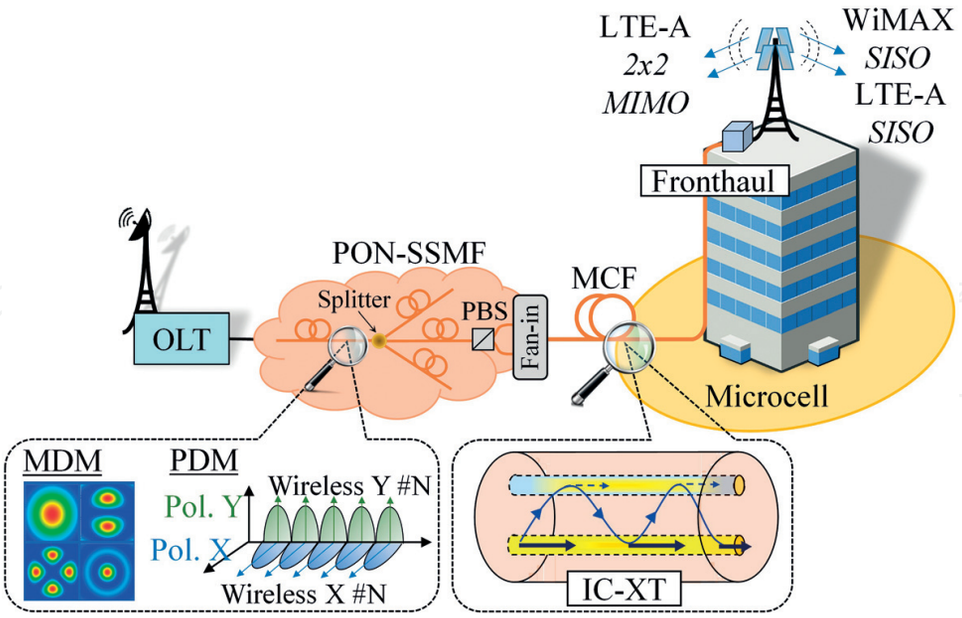

Figure 8. Next-generation optical fronthaul system using MCF medium operating with a converged fiber-wireless PON including optical polarization-division multiplexing (PDM) and mode-division multiplexing (MDM) transmissions.

Figure 8 depicts the proposed fronthaul provision applied to converged fiber-wireless PON including PDM to provide connectivity between the SSMF and MCF media.

Remarkably, the use of MCFs in the next-generation RoF fronthaul systems is proposed for the first time in [52, 87]. In these works, it is investigated the performance of fully standard LTE-A signals in MIMO and SISO configurations with the random IC-XT fluctuations and the demonstration of fronthaul provision of both LTE-A and WiMAX signals using a 150-m SI-SM-HO-UC-LB-4CF. In order to reduce the random fluctuations of the error vector magnitude (EVM) induced by the IC-XT, the core interleaving nonlinear stimulation (CINLS) was proposed to mismatch the phase constant of adjacent core modes reducing the temporal and spectral EVM fluctuations of the MCF-RoF transmissions.

4.2. Signal processing

The potential application of MCFs is not only restricted to SDM transmissions. The inherent capability of a MCF to modify the propagated signals allows us to investigate a vast scenario of new applications for ultra-high capacity SDM transmissions and microwave photonics (MWP) based on signal processing techniques. As we will see, the basic concept of the signal processing using MCFs is a far richer scope than initially foreseen.

In particular, the use of MCFs for MWP applications based on signal processing was firstly proposed by Gasulla and Capmany in [88]. In this work the authors investigate the suitability of these new fibers to perform true-time delay lines (TTDLs), optical beamforming, optical filtering and arbitrary waveform generation using heterogeneous cores. These applications have been extensively researched in [30, 31, 89–93] with different MCF designs and experimental setups. As an attractive example, it should be remarked the proposal reported in [31, 90], where the inscription of selective Bragg gratings in a homogeneous MCF it was introduced in [90] and

experimentally verified in [31] to achieve compact fiber-based TTDL without using heterogeneous cores. Along this line, other MWP applications such as optical beamforming can also be performed by using homogeneous cores as described in [94]. In this work, Llorente and coworkers propose a compact all-fiber beamformer based on a *N*-core homogeneous MCF.

On the other hand, the MCF signal processing also involves additional applications and functionalities such as pulse shaping, dispersion engineering, modal conversion and modal filtering applications. Remarkably, the engineering of the refractive index profile allows us to implement these fashion features in MCF media. In this scenario, a fascinating proposal recovered from the string and quantum field theory was firstly introduced in [95] within the framework of photonics and further developed in [19, 96] to design SCFs and MCFs: the supersymmetry (SUSY). Specifically, one-dimensional SUSY allows us to perform the aforementioned MWP applications. The specific details can be found in [96] for cylindrical potentials with axial symmetry. As an interesting example (among other applications detailed in this work), we include here the description of a true modal (de)multiplexer (M-MUX/DEMUX) using a 3-core MCF. **Figure 9** shows the optical device and its functionality.

The device is designed using a 60-cm MCF comprising three cores *a*, *b* and *c* with a core-to-core distance $d_{ab} = d_{ac} = 55$ μm, $R_0 = 25$ μm, and $\lambda_0 = 1550$ nm [**Figure 9(a)**]. The index profiles of the cores *a* and *c* are calculated by using the Darboux procedure. The index profile of the core *b* is taken to be the step-index profile, with $n_b = 1.45$ when $r < R_0$. A 10-ps Gaussian optical pulse is launched to the central core *b*, first in the LP_{01} mode, and later in the LP_{11} and LP_{21} modes with a peak power of 0 dBm. The numerical simulation was performed using a beam propagation method at $\lambda_0 = 1550$ nm. **Figure 9(b)** shows the numerical results of the optical pulse propagating through each LP mode in the M-DEMUX. It is worth noting that, in contrast with other mode (de)multiplexing strategies [97–100], a true mode demultiplexing is achieved for each LP mode. At the device output, the pulse launched into the LP_{11} mode of the core *b* is found in the LP_{11} mode of the core *a*, the pulse launched into the LP_{01} mode of the core *b* is found in the same mode and core, and the pulse launched into the LP_{21} mode of the core *b* can be observed

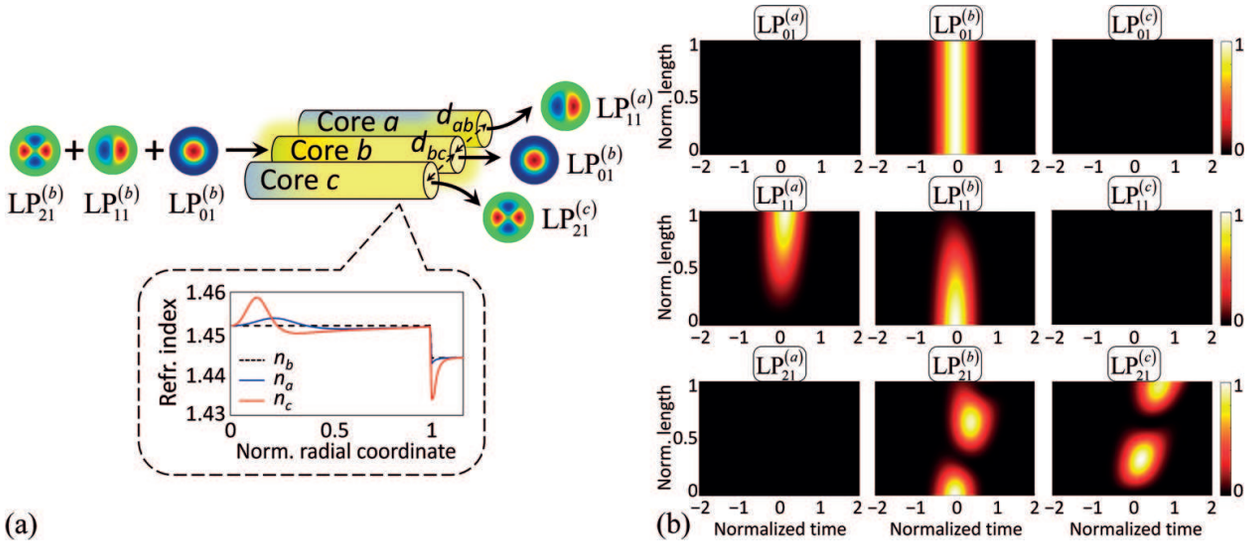

Figure 9. Modal (de)multiplexer based on a 60-cm 3-core MCF [96]. (a) Schematic structure of the optical device. (b) A 10-ps Gaussian pulse propagating through the: LP_{01}, LP_{11} and LP_{21} modes of the cores *a*, *b*, and *c*.

in the LP_{21} mode of the core *c*. Moreover, pulse shaping and dispersion engineering functionalities can be incorporated in the proposed device as indicated in [96]. On the other hand, it should be noted that the SUSY transformations presented in [96] can also be applied to axially symmetric quantum and acoustic potentials as discussed in this work.

4.3. Multi-core fiber lasers, amplifiers and optical sensors

All-fiber designs of optical lasers, amplifiers and sensors using MCFs have been extensively investigated in recent years [32, 101–111]. In particular, the multi-mode interference (MMI) which can be observed through a chain SMF-MCF-SMF is widely employed in lasers, amplifiers and optical sensors to improve the performance of classical designs based on SCFs [32, 104].

As one can expect, the basic concept of an active MCF is the natural evolution for the cladding pumped rare-earth-doped fibers. The classical design using a single core offers an excellent combination of high efficiency and beam quality. However, high output powers are limited by the stimulation of nonlinear effects. In that case, the increment of the mode field area is the obvious solution to decrease the nonlinear effects. In this scenario, active MCFs offer the possibility of reducing the nonlinear effects using a coupled-core design to generate supermodes with large mode field area [101, 105]. Moreover, note that the gain medium is split at discrete regions (cores) inside the cladding, and therefore, the thermal dissipation is higher than in the classical single-core design. As a result, higher output powers can be achieved in MCF media [105]. On the other hand, in contrast with a SCF bundle, a *N*-core MCF laser/amplifier only requires a single pumped laser for *N* optical paths, with the corresponding energy cost reduction for the network operators [5, 106, 107].

In this topic, an intense research work has been developed in the last decade [5, 11, 12]. To date, most CC-MCF lasers/amplifiers operate in the in-phase supermode combining high brightness and near-diffraction limited far field profile. The selection of the in-phase supermode can be performed by using diverse methods such as phase-locking and Talbot cavities [102]. As an example, a monolithic fiber laser using a CC-MCF with highly and lowly reflective fiber Bragg gratings (HR/LR-FBG) is shown in **Figure 10(a)** [104]. The MCF segment is located between the HR-FBG and the LR-FBG creating an active cavity, where the MMI allows us to obtain a high-contrast spectral modulation. In addition, the uniform illumination of the cores is achieved by performing a cladding pumping scheme. Remarkably, this MCF laser design demonstrates the direct correlation between the MMI in few-mode SCF systems and in the laser operation when multiple supermodes oscillate simultaneously. Following a similar approach, additional MCF laser and amplifier designs have been proposed in [103, 105]. Nevertheless, in long-haul SDM transmissions the usual design is the multi-core erbium-doped-fiber-amplifier based on a cladding pumped scheme [106, 107].

On the other hand, MCF sensors are also based on a similar concept as in the laser of the previous example [see **Figure 10(b)**]. The sensor comprises two SSMFs spliced to a short MCF segment with hexagonal shaped cores. The operating principle within the MCF segment is the MMI, which induces a deep peak in the transmission spectrum. An external environmental change shifts the spectral position of the minimum. As an specific example, let us consider a temperature change. When increasing the temperature, the thermal expansion of the MCF medium will increase the refractive index of the silica cores, and consequently, the peak will be shifted to a longer wavelength [32].

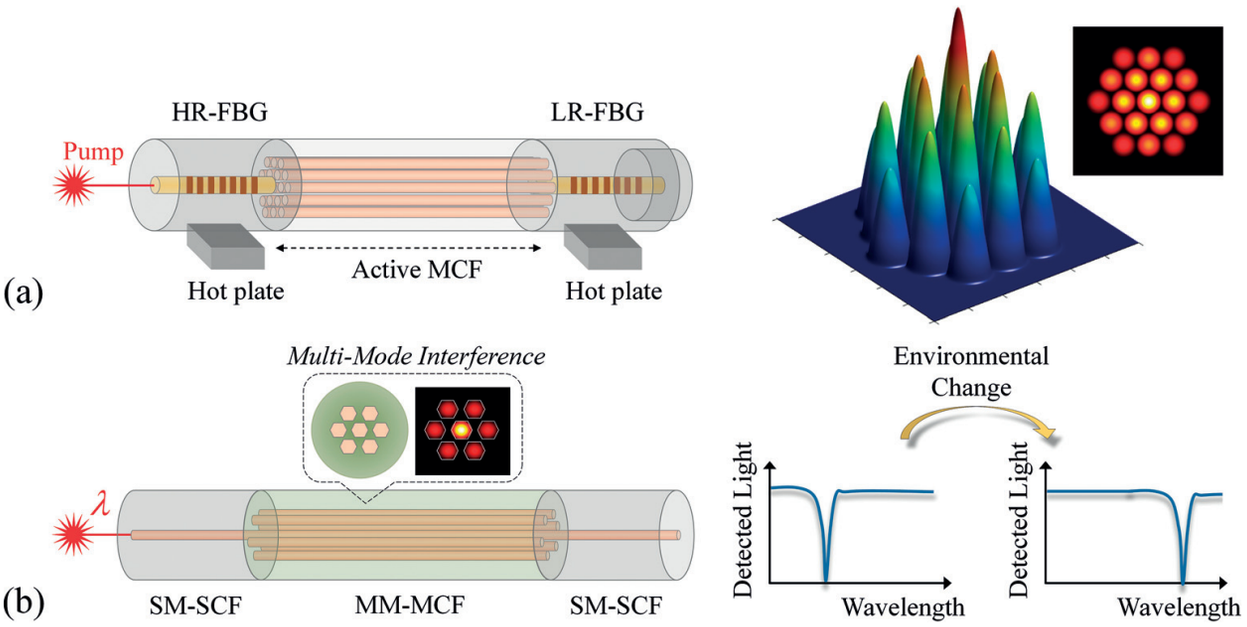

Figure 10. MCF laser and optical sensor operating on the principle of multi-mode interference (MMI). (a) MCF laser comprising a highly and lowly reflective fiber Bragg grating (HR/LR-FBG). (b) MCF optical sensor with hexagonal shaped cores. Results based on [32, 104].

In the past, fiber optic sensors using SCFs have been widely discussed for sensing in a broad range of industrial and scientific applications including temperature, force, liquid level, pressure and acoustic waves, among other. Nowadays, the MCF technology allows us to design and fabricate new optical sensors providing accuracy, high resolution, compactness, stability, reproducibility and reliability [32, 108–111].

4.4. Multi-core fibers for medical applications

Multi-core optical fibers have also been studied in recent years within the context of medicine for biomedical sensing and imaging applications [112–121]. Basically, biomedical sensors using MCFs are based on the MMI technique previously described. Thus, let us now focus our attention on biomedical imaging applications in the next paragraphs.

Nowadays, the main challenge in biomedical imaging is the study of cells in biological tissues. In this scenario, the multiphoton microscopy and adaptive optics become fundamental technologies because of their benefits in cellular resolution, high sensitivity, and high imaging rate [121]. In particular, the two-photon excited fluorescence (TPEF) microscopy requires the use of adaptive optics to increase the imaging depth, in practice limited to 1 mm [122]. Remarkably, the so-called *lensless endoscope* is based on the TPEF microscopy and adaptive optics adding at the same time the use of an optical waveguide [121]. The waveguide should be capable of acquiring a multiphoton image of an object located at its tip. To this end, MCFs have been proposed as a necessary technology for the realization of ultrathin lensless endoscopes [112–121]. **Figure 11** depicts different MCF types proposed for biomedical imaging along with a basic scheme of adaptive optics using a spatial light modulator (SLM).

In general, MCFs used for image transport require a high number of cores (>100) with low IC-XT levels and low intermodal dispersion among cores. Therefore, the preferred design is a SI-SM-HO-CC-LB-MCF, in line with the MCF shown in **Figure 11(a)**. Examples of this MCF type fabricated for medical imaging purposes can be found in [113–115], with $d_{ab} < 20$ μm and IC-XT levels lower than −20 dB/m. In spite of the fact that the intermodal dispersion can be reduced with a homogeneous design, disordered MCFs based on the transverse Anderson localization have been reported in [22] to improve the image transport quality [see **Figure 11(b)**]. Specifically, the transverse Anderson localization of light allows localized optical-beam-transport through a transversely disordered medium. Interesting, in disordered multi-dielectric media, the resultant image quality can also be understood with the perturbation theory. In general, disordered arranged non-homogeneous cores exhibit a high phase-mismatching between their LP modes. As a result, the IC-XT level between adjacent core modes is found to be of the same order or lower than in a homogeneous and periodically arranged design [**Figure 11(a)**]. In a similar way and from our viewpoint, additional highly density MCF designs could be investigated from the CLMT using HB cores with a random orientation of the principal axes to minimize the IC-XT.

On the other hand, adaptive optics is required in the TPEF microscopy to recover the initial imaging of the biological tissue [**Figure 11(c)**]. The advance on wave front shapers composed by 2-D SLMs and deformable mirrors have spurred the main evolution in ultrathin endoscopes [121]. Thompson et al. were the first to report imaging with a lensless endoscope based on a waveguide with multiple cores [112]. Later, in 2013, Andresen and co-workers realized a lensless endoscope employing a MCF similar to **Figure 11(a)** with extremely low IC-XT between adjacent cores [113]. In the same line, additional works have been reported combining MCF and MM-SCFs with adaptive optics in [114–120]. At present, the major aim in lensless endoscopy using MCF media is to increase the core density with a reduced IC-XT and intermodal dispersion between neighboring cores [121].

4.5. Multi-core fiber opportunities in experimental physics

In the past, fiber-optical analogies have been investigated to use optical fibers as an experimental platform for testing different physical phenomena in various fields, such as in quantum

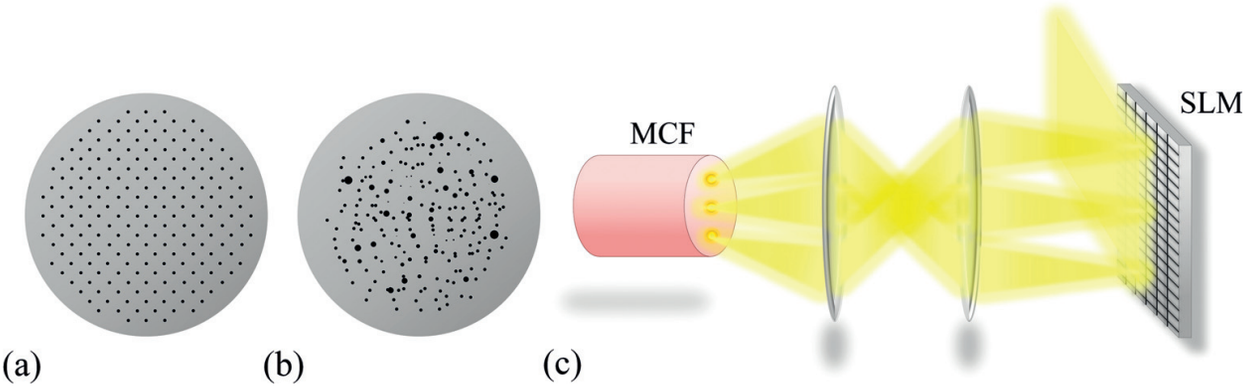

Figure 11. MCFs and adaptive optics for medical imaging. (a) MCF with low IC-XT and periodically arranged cores [113], (b) disorder MCF based on transverse Anderson localization, and (c) wavefront shaping with a single spatial light modulator (SLM) for a MCF based lensless endoscope. Results based on [22, 114].

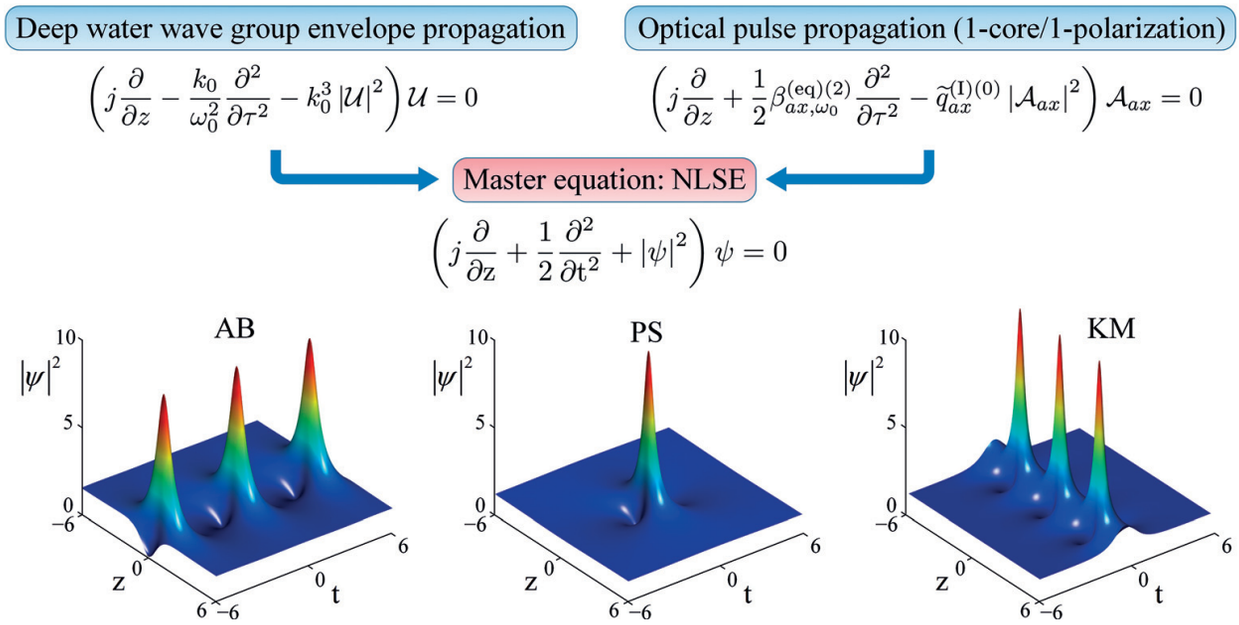

Figure 12. Analogy between fluid mechanics and optics. The NLSE describes the linear and nonlinear wave propagation in different physical systems. Analytical SFB solutions of the NLSE: Akhmediev breathers (ABs), the Peregrine soliton (PS) and the Kuznetsov-Ma (KM) solitons.

mechanics, general relativity or condensed matter physics, among others [16–23]. In fact, a specific example of solid-state physics has already been discussed in the previous subsection, the Anderson effect, relying on the immobility of an electron in a disordered lattice [21, 22]. As Anderson localization involves an interfering phenomenon, this effect has been extended to optics. In [21], Anderson localization has been discussed in two-dimensional photonic lattices, and in [22] it has been discussed its potential applications for medical imaging using disordered MCFs, as pointed out before. More broadly, additional strong disorder phenomena in optics such as the self-organized instability in MM-SCFs [123] can be generalized to MM-MCFs.

Another interesting example can be found in fluid dynamics in the studio of rogue waves on deep water. The giant oceanic rogue waves emerge from the sea induced by many different linear and nonlinear wave propagating effects [124]. Indeed, these nonlinear phenomena can be investigated from a fiber-optical analogy [125]. The nonlinear wave propagation on deep water and in a SM-SCF is described in both cases by a master equation: the nonlinear Schrödinger equation (NLSE), as shown in **Figure 12**.

It can be seen that both propagating equations present a similar form, and therefore, the theoretical results can be directly extrapolated from one field to another. Significantly, the emergence of rogue waves can be analytically studied from the solutions of the NLSE referred to as *solitons on finite background* (SFB) [126]. As a specific example, we include in **Figure 12** the Akhmediev breathers (ABs), the Peregrine soliton (PS) and the Kuznetsov-Ma (KM) solitons[21]. In a similar way, the coupled NLSEs (CNLSEs) have also been discussed in the literature to gain physical

[21]Many of these SFB solutions are termed in the literature as rogue waves. Nevertheless, the fundamental concept of rogue waves emerging unexpectedly from the sea requires additional statistical criteria only fulfilled by higher-order SFB solutions. In either case, the term rogue waves is commonly used for any analytical SFB solution of the NLSE.

insight between interacting rogue waves [127–130]. In this scenario, MCFs offer the possibility of investigating the collision of these nonlinear solutions by using the CLMT [Eq. (14)]. In fact, MCFs can be employed to elucidate the underlying wave propagation phenomena of any physical system with propagating equations of the form of the CNLSEs, for example, superposed nonlinear waves in coherently coupled Bose-Einstein condensates [130] or turbocharge applications in acoustics [131]. Remarkably, in acoustics, the CLMT reported in [60] can play an essential role. Time-varying multi-core cylindrical acoustic ducts can be engineered with the same modal properties as optical MCFs. Therefore, the presented theory can be employed to analyze the intermodal dispersion and the random medium perturbations in acoustic duct conductions.

On the other hand, additional exotic physical phenomena can also be explored in MCF media expanding the possibilities of the classical SCFs. For example, an optical pulse propagating through a SCF establishes a moving medium which corresponds to a space-time geometry. Specifically, this gravitational approach was employed in [20] to demonstrate a fiber-optical analogy of the event horizon in a black hole. Along this line, additional gravitational anomalies could be investigated in a MCF when adjacent cores perturb the space-time geometry created by an optical pulse propagating in a given core of the fiber.

Finally, it is worth mentioning that MCFs are being explored in other branches of experimental physics as in astronomy [132]. The main advantage of these new fibers is the reduced core-to-core distance which can be achieved in a single cladding. In particular, this property has revealed special interest because of the superior fill factor[22] to other approaches for creating spectroscopic maps of galaxies or detecting exoplanets. The Sydney-AAO Multi-object Integral field spectrograph (SAMI) project [133], responsible of performing a large spatial spectroscopy of galaxies, pioneered the introduction of MCFs in astronomical observatories.

5. Conclusions and outlook

Multi-core optical fibers have been developed during the last decade, remarkably within the context of SDM transmissions. In this chapter we have reviewed the main MCF types, the fundamental concepts of the linear and nonlinear propagation, and finally, their potential applications in diverse fields of science. In spite of the fact that the fundamentals of the MCF technology have been well elucidated in recent years, the main challenges in this topic involve the following points:

- The analysis of the longitudinal and temporal fluctuations of the crosstalk should be further investigated in the multi-mode regime. To this end, the CLMT of [61] could be extended to MM-MCFs. In addition, other theoretical models based on the Manakov equations [56, 57] can also be employed and extended to the femtosecond regime.
- Existing and additional MCF fabrication methods should be explored and optimized not only in the S + C + L optical bands, but also in the first and second transmission window. In general, the manufacturing cost of a MCF and the peripheral devices (fan-in/fan-out

[22]Fill factor: ratio between the cores and the total transversal area of the waveguide. Typically, in MM-SCFs (105/125) the fill factor is of the order of 0.7. Using a MM-SCF or a fiber bundle of SM-SCFs a lot of dead space cannot be observed.

connectors, lasers, amplifiers, photonic lanterns, power combiners, couplers, multiplexers, etc) should be reduced.

- The efforts in future MCF designs must be focused on the increment of the core density minimizing the IC-XT, the intermodal dispersion and the random linear birefringence induced by the microbends. The impact of external perturbations such as the macrobends and the fiber twisting should also be reduced in real-deployed MCF systems. Furthermore, new MCF designs should also be investigated for lensless endoscope integrating a high number of cores with a reduced evanescent field in the cladding. In this scenario, it has been proposed HB-MCFs with a random orientation of the principal axes in each core.
- Fronthaul connectivity performed by MCF-ROF transmissions should be spurred for the next-generation wireless systems, e.g. 5G cellular technology and Beyond-5G. In this line, selective-inscribed FBGs [31] and SUSY MCFs [96] will allow us to process the propagated optical signals between the OLT and the microcell.
- On-line MIMO processing of MDM transmissions using MM-MCFs should be developed to support real-time applications in backbone and access networks [134].
- Quantum communications are emerging as a fundamental key in network security [135]. Nowadays, quantum key distribution (QKD) is making the transition from the laboratory to field trials [136]. In this scenario, the QKD through MCF media should be further investigated for the next-generation optical SDM networks [137].

Acknowledgements

This work was supported by Spanish National Plan projects MINECO/FEDER UE XCORE TEC2015-70858-C2-1-R and HIDRASENSE RTC-2014-2232-3. A. Macho work was supported by BES-2013-062952 F.P.I. Grant.

Author details

Andrés Macho Ortiz* and Roberto Llorente Sáez

*Address all correspondence to: amachor@ntc.upv.es

Nanophotonics Technology Center, Universitat Politècnica de València, Valencia, Spain

References

[1] Ayhan Y, Cavdar IH. Optimum link distance determination for a constant signal to noise ratio in M-ary PSK modulated coherent optical OFDM systems. Telecommunication Systems. 2013;**4**:461-470

[2] Yu J, Dong Z, Chien H-C, Jia Z, Li X, Huo D, Gunkel M, Wagner P, Mayer H, Schippel A. Transmission of 200 G PDM-CSRZ-QPSK and PDM-16QAM with a SE of 4 b/s/Hz. Journal of Lightwave Technology. 2013;**31**(4):515-522

[3] Li L, Jijun Z, Degong D, Aihan Y. Analysis modulation formats of DQPSK in WDM-PON system. Optik. 2012;**123**:2050-2055

[4] Essiambre R-J, Kramer G, Winzer PJ, Foschini GJ, Goebel B. Capacity limits of optical fiber networks. Journal of Lightwave Technology. 2010;**28**(4):662-701

[5] Richardson D, Fini J, Nelson LE. Space-division multiplexing in optical fibres. Nature Photonics. 2013;**7**:354-362

[6] Bozinovic N et al. Terabit-scale orbital angular momentum mode division multiplexing in Fibers. Science. 2013;**340**(6140):1545-1548

[7] Van Uden RGH et al. Ultra-high-density spatial division multiplexing with a few-mode multi-core fibre. Nature Photonics. 2014;**8**:865-870

[8] Inao S et al. High density multi-core-fibre cable. In: The International Cable Connectivity Symposium (IWCS). 1979. pp. 370-384

[9] Inao S, Sato T, Sentsui S, Kuroha T, Nishimura Y. Multi-core optical fiber. In: The Optical Fiber Communication Conference and Exhibition (OFC). Washington: Optical Society of America; 1979. WB1

[10] Berdagué S, Facq P. Mode-division multiplexing in optical fibers. Applied Optics. 1982;**21**(11):1950-1055

[11] Saitoh K, Matsuo M. Multicore Fiber technology. Journal of Lightwave Technology. 2016;**34**(1):55-66

[12] Mizuno T, Takara H, Sano A, Miyamoto Y. Dense space-division multiplexed transmission systems using multi-core and multi-mode fiber. Journal of Lightwave Technology. 2016;**34**(2):582-591

[13] Temprana E et al. Overcoming Kerr-induced capacity limit in optical fiber transmission. Science. 2015;**348**(6242):1445-1447

[14] Li G, Bai N, Zhao N, Xia C. Space-division multiplexing: The next frontier in optical communication. Advanced in Optics and Photonics. 2014;**6**:413-487

[15] Puttnam BJ et al. Modulation formats for multi-core fiber transmission. Optics Express. 2014;**22**(26):32457-32469

[16] Wan W, Jia S, Fleischer JW. Dispersive superfluid-like shock waves in nonlinear optics. Nature Physics. 2007;**3**:46-51

[17] Fatome J, Finot C, Millot G, Armaroli A, Trillo S. Observation of optical undular bores in multiple four-wave mixing. Physical Review X. 2014;**4**:021022

[18] Dreisow F et al. Classical simulation of relativistic Zitterbewegung in photonic lattices. Physical Review Letters. 2010;**105**:143902

[19] Miri M-A, Heinrich M, Ganainy RE, Christodoulides DN. Supersymmetric optical structures. Physical Review Letters. 2013;**110**:233902

[20] Philbin TG et al. Fiber-optical analog of the event horizon. Science. 2008;**319**(5868):1367-1370

[21] Scwartz T, Bartal G, Fishman S, Segev M. Transport and Anderson localization in disordered two-dimensional photonic lattices. Nature. 2007;**446**:52-55

[22] Karbasi S et al. Image transport through a disordered optical fibre mediated by transverse Anderson localization. Nature Communications. 2014;**5**(3362)

[23] Saleh MF et al. Raman induced temporal condensed matter physics in a gas-filled photonic crystal fibers. Optics Express. 2015;**23**(9):11879-11886

[24] Sumimoto Electric. Sumitomo electric has developed new-type multi-Core optical Fiber for optical interconnects and realized highest-density multi-Core Fiber optic cable [internet]. March 26, 2015. Available from: http://global-sei.com/company/press/2015/03/prs022_s.html

[25] Xia C, Bai N, Ozdur I, Zhou X, Li G. Supermodes for optical transmissions. Optics Express. 2011;**19**(17):16653-16664

[26] Ryf R et al. Space-division multiplexed transmission over 3 × 3 coupled-core multicore fiber. In: Optical Fiber Communication Conference (OFC). San Francisco: Optical Society of America; 2014. Tu2J.4

[27] Hayashi T et al. Coupled-core multi-core fibers: High-spatial-density optical transmission fibers with low differential modal properties. In: European Conference On Optical Communications (ECOC); Valencia. IEEE. 2015

[28] Stone JM, Yu F, Knight JC. Highly birefringent 98-core fiber. Optics Letters 2014; **39**(15): 4568-4570

[29] Kim Y et al. Adaptive multiphoton Endomicroscope incorporating a polarization-maintaining multicore optical fibre. IEEE Journal of Selected Topics in Quantum Electronics. 2016;**22**(3):171-178

[30] García S, Gasulla I. Dispersion-engineered multicore fibers for distributed radio-frequency signal processing. Optics Express. 2016;**24**(18):20641-20654

[31] Gasulla I, Barrera D, Hervás J, Sales S. Spatial division multiplexed microwave signal processing by selective grating inscription in homogeneous multicore fibers. Scientific Reports. 2017;**7**(41727). https://www.nature.com/articles/srep41727

[32] López JEA, Eznaveh ZS, LiKamWa PL, Schülzgen A, Correa RA. Multicore fiber sensor for high-temperature applications up to 1000°C. Optics Letters. 2014;**39**(15):4309-4312

[33] Hayashi T, Taru T, Shimakawa O, Sasaki T, Sasaoka E. Design and fabrication of ultra-low crosstalk and low-loss multi-core fiber. Optics Express. 2011;**19**(17):16576-16592

[34] Ziolowicz A et al. Hole-assisted multicore optical fiber for next generation telecom transmission systems. Applied Physics Letters. 2014; **105**(081106)

[35] Mahdiraji GA, Amirkhan F, Chow DM, Kakaie Z, Yong PS, Dambul KD, Adikan FRM. Multicore flat Fiber: A new fabrication technique. IEEE Photonics Technology Letters. 2014;**26**(19):1972-1974

[36] Ishida I et al. Possibility of stack and draw process as fabrication technology for multi-core fiber. In: Optical Fiber Communication Conference (OFC). Anaheim: Optical Society of America; 2013. OTu2G.1

[37] Yamamoto J et al. Fabrication of multi-core fiber by using slurry casting method. In: Optical Fiber Communication Conference (OFC). Los Angeles: Optical Society of America; 2017. Th1H.5

[38] Feuer M et al. Joint digital signal processing receivers for spatial superchannels. IEEE Photonics Technology Letters. 2012;**24**(21):1957-1960

[39] Eriksson TA et al. Single parity check-coded 16QAM over spatial superchannels in multicore fiber transmission. Optics Express. 2015;**23**(11):14569-14582

[40] Rademacher G, Puttnam BJ, Luis RS, Awaji Y, Wada N. Experimental investigation of a 16-dimensional modulation format for long-haul multi-core fiber transmission. In: European Conference on Optical Communications (ECOC). Valencia: IEEE; 2015. P.5.10

[41] Puttnam BJ, Luis RS, Mendinueta JMD, Awaji Y, Wada N. Linear block-coding across >5 Tb/s PDM-64QAM spatial super-channels in a 19-core fiber. In: European Conference on Optical Communications (ECOC). Valencia: IEEE; 2015. P.5.6

[42] Marcuse D. Theory of Dielectric Optical Waveguides. Elsevier; 1974

[43] Winzer PJ, Essiambre R-J. Advanced modulation formats for high-capacity optical transport networks. Journal of Lightwave Technology. 2006;**24**(12):4711-4728

[44] Gloge D. Weakly guiding fibers. Applied Optics. 1971;**10**(10):2252-2258

[45] Fini JM, Zhu B, Taunay TF, Yan MF. Statistics of crosstalk in bent multicore fibers. Optics Express. 2010;**18**(14):15122-15129

[46] Koshiba M, Saitoh K, Takenaga K, Matsuo S. Multi-core fiber design and analysis: Coupled-mode theory and coupled-power theory. Optic Express. 2011;**19**(26):B102-B111

[47] Koshiba M, Saitoh K, Takenaga K, Matsuo S. Analytical expression of average power-coupling coefficients for estimating intercore crosstalk in multicore fibers. IEEE Photonics Journal. 2012;**4**(5):1987-1995

[48] Hayashi T, Sasaki T, Sasaoka E, Saitoh K, Koshiba M. Physical interpretation of intercore crosstalk in multicore fiber: Effects of macrobend, structure fluctuation, and microbend. Optics Express. 2013;**21**(5):5401-5412

[49] Macho A, Morant M, Llorente R. Experimental evaluation of nonlinear crosstalk in multi-core fiber. Optics Express. 2015;**23**(14):18712-18720

[50] Macho A, Morant M, Llorente R. Unified model of linear and nonlinear crosstalk in multi-core fiber. Journal of Lightwave Technology. 2016;**34**(13):3035-3046

[51] Ye F, Tu J, Saitoh K, Morioka T. Simple analytical expression for crosstalk estimation in homogeneous trench-assisted multi-core fibers. Optics Express. 2014;**22**(19):23007-23018

[52] Morant M, Macho A, Llorente R. On the suitability of multicore fiber for LTE-advanced MIMO optical fronthaul systems. Journal of Lightwave Technology. 2016;**34**(2):676-682

[53] Macho A, Meca CG, Peláez FJF, Morant M, Llorente R. Birefringence effects in multi-core fiber: Coupled local-mode theory. Optics Express. 2016;**24**(19):21415-21434

[54] Iizuka K. Elements of photonics volume I. Wiley; 2002

[55] Luis RS et al. Time and modulation frequency dependence of crosstalk in homogeneous multi-core fibers. Journal of Lightwave Technology. 2016;**34**(2):441-447

[56] Mecozzi A, Antonelli C, Shtaif M. Nonlinear propagation in multi-mode fiber in the strong coupling regime. Optics Express. 2012;**20**(11):11673-11678

[57] Mumtaz S, Essiambre RJ, Agrawal GP. Nonlinear propagation in multimode and multicore fibers: Generalization of the Manakov equations. Journal of Lightwave Technology. 2013;**31**(3):398-406

[58] Chiang KS. Coupled-mode equations for pulse switching in parallel waveguides. IEEE Xplore: IEEE Journal of Quantum Electronics. 1997;**33**(6):950-954

[59] Liu M, Chiang KS. Effects of intrapulse stimulated Raman scattering on short pulse propagation in a nonlinear two-core fiber. Applied Physics B. 2007;**87**:45-52

[60] Liu M, Chiang KS. Pulse propagation in a decoupled two-core fiber. Optics Express. 2010;**18**(20):21261-21268

[61] Macho A, Meca CG, Peláez FJF, Cortés-Juan F, Llorente R. Ultra-short pulse propagation model for multi-core fibers based on local modes. Scientific Reports. 2017;**7**(16457)

[62] Weiner AM. Ultrafast optics. Wiley; 2009

[63] Agrawal GP. Nonlinear fiber optics. Elsevier; 2013

[64] Zhu B, Taunay T, Yan M, Fini J, Fishteyn M, Monberg EM. Seven-core multi-core fibre transmissions for passive optical network. Optics Express. 2010;**18**(11):11117-11122

[65] Puttnam BJ, Delgado J-M, Sakaguchi J, Luis RS, Klaus W, Awaji Y, Wada N, Kanno A, Kawanishi T. 210Tb/s Self-Homodyne PDM-WDM-SDM Transmission with DFB Lasers in a 19-Core Fibre. In: European Conference on Optical Communications (ECOC). London: IEEE; 2013. TuC1.2

[66] Sakaguchi J et al. 305 Tb/s space division multiplexed transmission using homogeneous 19-Core fibre. Journal of Lightwave Technology. 2013;**31**(4):554-562

[67] Takara H et al. 1.01-Pb/s (12 SDM/222 WDM/456 Gb/s) crosstalk-managed transmission with 91.4-b/s/Hz aggregate spectral efficiency. In: European Conference on Optical Communications (ECOC). Amsterdam, Netherlands: IEEE; 2012. Th3.C.1

[68] Chandrasekhar S et al. WDM/SDM transmission of 10 x x128-Gb/s PDM-QPSK over 2688-km 7-core fiber with a per-fiber net aggregate spectral-efficiency distance product of 40,320 km·b/s/Hz. In: European Conference on Optical Communications (ECOC). Geneva, Switzerland: IEEE; 2011. Th13.C.4

[69] Takeshima K et al. 51.1-Tbit/s MCF transmission over 2520 km using cladding pumped 7-core EDFAs. In: Optical Fiber Communication Conference (OFC). Los Angeles, USA: Optical Society of America; 2015. W3G.1

[70] Sakaguchi J et al. Realizing a 36-core, 3-mode Fibre with 108 Spatial Channels. In: Optical Fiber Communication Conference (OFC). Los Angeles, USA: Optical Society of America; 2015. Th5C.2

[71] Shibahara K, et al. Dense SDM (12-core x 3-mode) Transmission over 527 km with 33.2 ns Mode-Dispersion Employing Low-Complexity Parallel MIMO Frequency-Domain Equalization. In: Optical Fiber Communication Conference (OFC). Los Angeles, USA: Optical Society of America; 2015. Th5C.3

[72] Igarashi K, et al. 114 Space-Division-Multiplexed Transmission over 9.8-km Weakly-Coupled-6-Mode Uncoupled-19-Core Fibers. In: Optical Fiber Communication Conference (OFC). Los Angeles, USA: Optical Society of America; 2015. Th5C.4

[73] Igarashi K et al. Ultra-dense spatial-division-multiplexed optical fiber transmission over 6-mode 19-core fibers. Optics Express. 2016;**24**(10):10213-10231

[74] Kobayashi T et al. 1-Pb/s (32 SDM/46 WDM/768 Gb/s) C-band dense SDM transmission over 205.6-km of single-mode heterogeneous multi-core fiber using 96-Gbaud PDM-16QAM channels. In: Optical Fiber Communication Conference (OFC). Los Angeles, USA: Optical Society of America; 2017. Th5B.1

[75] Tanaka K, Agata A. Next-generation Optical Access Networks for C-RAN. In: Optical Fiber Communication Conference (OFC). Los Angeles, USA: Optical Society of America; 2015. Tu2E.1

[76] Cvijetic N. Optical network evolution for 5G mobile applications and SDN-based control. In: Proceedings of 16th International Telecomm. Network Strategy and Planning Symposium. IEEE; 2014

[77] Öhlen P et al. Flexibility in 5G Transport Network: The Key to Meeting the Demand for Connectivity [Internet]. 2015. Available from: https://www.ericsson.com/

[78] Rappaport TS. Millimeter wave wireless communications for 5G cellular: It will work! In: Personal, indoor, and mobile radio communications conference. Washington, USA: IEEE. 2014

[79] Ericsson. 5G Energy Performance [Internet]. 2015. Available from: http://www.5gamericas.org/files

[80] Kohn U. Fronthaul Networks–a Key Enabler for LTE-Advanced [Internet]. 2014. Available from: https://oristel.com.sg/wp-content/uploads/2015/03/Fronthaul-Networks-A-Key-Enabler-for-LTE-Advanced.pdf

[81] Zhu M, Liu X, Chand N, Effenberger F, Chang G-K. High-capacity mobile fronthaul supporting LTE-Advanced carrier aggregation and 8×8 MIMO. In: Optical Fiber Communication Conference (OFC). Optical Society of America; 2015. M2J.3

[82] Cheng L, Liu X, Chand N, Effenberger F, Chang G-K. Experimental demonstration of sub-Nyquist sampling for bandwidth- and hardware-efficient mobile fronthaul supporting 128×128 MIMO with 100-MHz OFDM signals. In: Optical Fiber Communication Conference (OFC). Anaheim, USA: Optical Society of America; 2016. W3C.3

[83] Wang N, Hossain E, Bhargava VK. Backhauling 5G small cells: A radio resource management perspective. IEEE Wireless Communications. 2015;**22**(5):41-49

[84] Morant, M., Macho, A., and Llorente, R. Optical fronthaul of LTE-Advanced MIMO by spatial multiplexing in multicore fiber. In: Optical Fiber Communication Conference (OFC). Optical Society of America; 2015. W1F.6

[85] Karadimitrakis A, Moustakas AL, Vivo P. Outage capacity for the optical MIMO channel, IEEE transactions on information theory. IEEE Transactions on Information Theory. 2014;**60**(7):4370-4382

[86] Sano A, Takara H, Moyamoto Y. Large capacity transmission systems using multi-core fibers. In: OptoElectronics and communication Conf. Melbourne, Australia: IEEE. 2014

[87] Macho A, Morant M, Llorente R. Next-generation optical fronthaul systems using multicore fiber media. Journal of Lightwave Technology. 2016;**34**(20):4819-4827

[88] Gasulla I, Capmany J. Microwave photonics applications of multicore Fibers. IEEE Photonics Journal. 2012;**4**(3):877-888

[89] Yu S, Jiang T, Li J, Zhang R, Wu G, Gu W. Linearized frequency doubling for microwave photonics links using integrated parallel Mach–Zehnder modulator. IEEE Photonics Journal. 2013;**5**(4):5501108

[90] Gasulla I, Barrera D, Sales S. Microwave photonic devices based on multicore fibers. In: Transparent Optical Networks (ICTON). Graz, Austria: IEEE; 2014. Th.B6.4

[91] Garcia S, Gasulla I. Design of heterogeneous multicore fibers as sampled true-time delay lines. Optics Letters. 2015;**40**(4):621-624

[92] Lawrence RC. Silicon Photonics for Microwave Photonics Applications. In: Optical Fiber Communication Conference (OFC). Anaheim, USA: Optical Society of America; 2016. M2B.4

[93] Wang J et al. Subwavelength grating enabled on-chip ultra-compact optical true time delay line. Scientific Reports. 2016;**6**:30235

[94] Zainullin A, Vidal B, Macho A, Llorente R. Multicore Fiber Beamforming Network for Broadband Satellite Communications. In: Proceedings of SPIE Terahertz, RF, Millimeter,

and Submillimeter-Wave Technology and Applications X. San Francisco, USA: SPIE; 2017. 1010310

[95] Chumakov SM, Wolf KB. Supersymmetry in Helmholtz optics. Physics Letters A. 1994;**193**:51-53

[96] Macho A, Llorente R, Meca CG. Supersymmetric transformations in optical fibers. Forthcoming

[97] Song KY, Hwang IK, Yun SH, Kim BY. High performance fused-type mode-selective coupler using elliptical core two-mode fiber at 1550 nm. IEEE Xplore: IEEE Photonics Technology. 2002;**14**(4):501-503

[98] Hanzawa N. Mode multi/demultiplexing with parallel waveguide for mode division multiplexed transmission. Optics Express. 2014;**22**(24):29321-29330

[99] Chang SH et al. Mode- and wavelength-division multiplexed transmission using all-fiber mode multiplexer based on mode selective couplers. Optics Express. 2015;**23**(6): 7164-7172

[100] Corral JL, Rodríguez DG, Llorente R. Mode-selective couplers for two-mode transmission at 850 nm in standard SMF. IEEE Photonics Technology Letters. 2016;**28**(4):425-428

[101] Michaille L, Bennet CR, Taylor DM, Shepherd TJ. Multicore photonic crystal Fiber lasers for high power/energy applications. IEEE journal of selected topics in. Quantum Electronics. 2009;**15**(2):328-336

[102] Anderson J, Jollivet C, Van Newkirk A, Schuster K, Grimm S, Schülzgen A. Multi-Core Fiber Lasers. In: Frontiers in Optics/Laser Science. Los Angeles, USA: Optical Society of America; 2015. LTu2H.2

[103] Chuncan W, Fan Z, Chu L, Shuiseng J. Microstructured optical fiber for in-phase mode selection in multicore fiber lasers. Optics Express. 2008;**16**(8):5505-5515

[104] Jollivet C et al. Mode-resolved gain analysis and lasing in multisupermode multi-core fiber laser. Optics Express. 2014;**22**(24):30377-30386

[105] Li L, Schülzgen A, Chen S, Témyanko VI. Phase locking and in-phase supermode selection in monolithic multicore fiber lasers. Optics Letters. 2006;**31**(17):2577-2579

[106] Krummrich PM, Akhtari S. Selection of energy optimized pump concepts for multi-core and multi-mode erbium doped fiber amplifiers. Optics Express. 2014;**22**(24):30267-30280

[107] Abedin KS et al. Multicore erbium doped Fiber amplifiers for space division multiplexing systems. Journal of Lightwave Technology. 2014;**32**(16):2800-2808

[108] Mizuno Y, Hayashi N, Tanaka H, Wada Y, Nahamura K. Brillouin scattering in multicore optical fibers for sensing applications. Scientific Reports. 2015;**5**:11388

[109] Newkirk AV, López JEA, Delgado GS, Piracha MU, Correa RA, Schülzgen A. Multicore Fiber sensors for simultaneous measurement of force and temperature. IEEE Photonics Technology Letters. 2015;**27**(14):1523-1526

[110] Newkirk AV, Eznaveh ZS, López J.EA, Delgado GS, Schülzgen A, Correa RA High Temperature Sensor based on Supermode Interference in Multicore Fiber. In: Conference on Lasers and Electro-Optics (CLEO). San Jose, USA: IEEE/OSA; 2014. SM2N.7

[111] Villatoro J, Arrizabalaga O, López JEA, Zubia J, de Ocáriz IS, Multicore Fiber Sensors. In: Optical Fiber Communication Conference (OFC). Los Angeles, USA: Optical Society of America; 2017. Th3H.1

[112] Thompson AJ et al. Adaptive phase compensation for ultracompact laser scanning endomicroscopy. Optics Letters. 2011;**36**(9):1707-1709

[113] Andresen ER et al. Toward endoscopes with no distal optics: Videorate scanning microscopy through a fiber bundle. Optics Letters. 2013;**38**(5):609-611

[114] Andresen ER et al. Two-photon lensless endoscope. Optics Express. 2013;**21**(18):20713-20721

[115] Andresen ER et al. Measurement and compensation of residual group delay in a multicore fiber for lensless endoscopy. Journal of the Optical Society of America B: Optical Physics. 2015;**32**(6):1221-1228

[116] Roper JC et al. Minimizing group index variations in a multicore endoscope fiber. IEEE Photonics Technology Letters. 2015;**27**(22):2359-2362

[117] Kim Y et al. Adaptive multiphoton endomicroscope incorporating a polarization-maintaining multicore optical fibre. IEEE Journal of Selected Topics in Quantum Electronics. 2015;**22**(3):6800708

[118] Sivankutty S et al. Extended field-of-view in a lensless endoscope using an aperiodic multicore fiber. Optics Letters. 2016;**41**(15):3531-3534

[119] Conkey DB et al. Lensless two-photon imaging through a multicore fiber with coherence-gated digital phase conjugation. Journal of Biomedical Optics. 2016;**21**(4):045002

[120] Stasio N, Moser C, Psaltis D. Calibration-free imaging through a multicore fiber using speckle scanning microscopy. Optics Letters. 2016;**41**(13):3078-3081

[121] Andresen ER et al. Ultrathin endoscopes based on multicore fibers and adaptive optics: A status review and perspectives. Journal of Biomedical Optics. 2016;**21**(12):121506

[122] Helmchen F, Denk F. Deep tissue two-photon microscopy. Nature Methods. 2005;**2**(12): 932-940

[123] Wright LG, Liu Z, Nolan DA, Li M-J, Christodoulides DN, Wise FW. Self-organized instability in graded-index multimode fibres. Nature Photonics. 2016;**10**:771-776

[124] Kharif C, Pelinovsky E. Physical mechanisms of the rogue wave phenomenon. European Journal of Mechanics. 2003;**22**:603-634

[125] Dudley JM, Dias F, Erkintalo M, Genty G. Instabilities, breathers and rogue waves in optics. Nature Photonics. 2014;**8**:755-764

[126] Akhmediev N, Korneev VI. Modulation instability and periodic solutions of the nonlinear Schrödinger equation. Theoretical and Mathematical Physics. 1986;**69**:1089-1093

[127] Wu CF, Grimshaw RH, Chow KW, Chan HNA. Coupled "AB" system: Rogue waves and modulation instabilities. Chaos. 2015;**25**:103113

[128] Zhong W-P, Belić M, Malomed BA. Rogue waves in a two-component Manakov system with variable coefficients and an external potential. Physical Review E. 2015;**92**:053201

[129] Manikandan K, Senthilvelan M, Kraenkel RA. On the characterization of vector rogue waves in two-dimensional two coupled nonlinear Schrödinger equations with distributed coefficients. The European Physical Journal B. 2016;**89**:218

[130] Mareeswaran RB, Kanna T. Superposed nonlinear waves in coherently coupled Bose–Einstein condensates. Physics Letters A. 2016;**380**:3244-3252

[131] Rämmal H, Lavrentjev J. Sound reflection at an open end of a circular duct exhausting hot gas. Noise control Engineering Journal. 2008;**56**(2):107-114

[132] Jovanovic N, Guyon O, Kawahara H, Kotani T. Application of Multicore Optical Fibers in Astronomy. In: Optical Fiber Communication Conference (OFC). Los Angeles, USA: Optical Society of America; 2017. W3H.3

[133] Croom S et al. The Sydney-AAO multi-object integral field spectrograph. MNRAS. 2012;**421**:872C

[134] Randel, S. et al. First Real-Time Coherent MIMO-DSP for Six Coupled Mode Transmission. In: IEEE Photonics Conference (IPC). Virginia, USA: IEEE; 2015. 15600579

[135] Scarani V, Bechmann-Pasquinucci H, Cerf NJ, Dušek M, Lütkenhaus N, Peev M. The security of practical quantum key distribution. Reviews of Modern Physics. 2009;**81**(3): 1301-1350

[136] Peev M et al. The SECOQC quantum key distribution network in Vienna. New Journal of Physics. 2009;**11**(7):075001

[137] Dynes JF et al. Quantum key distribution over multicore fiber. Optics Express. 2016;**24**(8): 8081-8087